Aquaculture 597 (2025) 741915

Contents lists available at ScienceDirect

Aquaculture

journal homepage: www.elsevier.com/locate/aquaculture

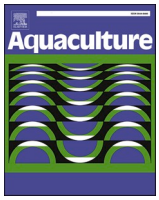

# Proteomic profiling of the *Macrobrachium rosenbergii* nodavirus infection: A study of early to late-stage infection *in vitro*

Ken Fong Chen [a], Wen Siang Tan [b], Lin Kooi Ong [a,c], Syafiq Asnawi Zainal Abidin [d,e], Iekhsan Othman [d,e], Beng Ti Tey [f], Ronald Fook Seng Lee [a,*]

[a] School of Pharmacy, Monash University Malaysia, Jalan Lagoon Selatan, 47500 Bandar Sunway, Selangor, Malaysia
[b] Department of Microbiology, Faculty of Biotechnology and Biomolecular Sciences, Universiti Putra Malaysia, 43400 Serdang, Selangor, Malaysia
[c] School of Health and Medical Sciences & Centre for Health Research, University of Southern Queensland, Toowoomba, QLD 4350, Australia
[d] Jeffrey Cheah School of Medicine and Health Sciences, Monash University Malaysia, Jalan Lagoon Selatan, 47500 Bandar Sunway, Selangor, Malaysia
[e] Proteomics and Metabolomics Platform, Monash University Malaysia, Jalan Lagoon Selatan, Bandar Sunway 47500, Selangor Darul Ehsan, Malaysia
[f] Chemical Engineering Discipline, School of Engineering, Monash University Malaysia, Jalan Lagoon Selatan, 47500 Bandar Sunway, Selangor, Malaysia

ARTICLE INFO

*Keywords:*
Giant freshwater prawn
*Macrobrachium rosenbergii* nodavirus
Proteomic analysis
Infection mechanism
Protein expression pathway

ABSTRACT

The *Macrobrachium rosenbergii* nodavirus (*Mr*NV), belonging to the *Nodaviridae* family, is responsible for a deadly infection in freshwater prawns, especially impacting the post-larvae of *Macrobrachium rosenbergii* with a mortality rate reaching 100 %. Recent research has shed light on the typical process of *Mr*NV trafficking within the host, illustrating how the virus navigates through cells as the infection advances and the subsequent cellular alterations. Yet, the specific cellular pathways disrupted by *Mr*NV, leading to these alterations, are underexplored. Furthermore, the precise effects of the *Mr*NV capsid protein, known for its strong immune response, on the host cells are not well understood. This study seeks to clarify these impacts by analysing and comparing the protein expression profiles in healthy, *Mr*NV virus-like particle (VLP) invaded, and *Mr*NV-infected Sf9 cells over a 24-h period using a mass spectrometry based proteomics approach. Our findings show that the protein expression in *Mr*NV VLP-invaded and *Mr*NV-infected Sf9 cells during the mid-infection stages is similar, involving key signalling pathways like the eukaryotic translation system, cell cycle, actin cytoskeleton regulation, and the mTOR pathway. However, changes in protein expression for key proteins such as 40S and 60S ribosomal subunits, 14–3-3 protein epsilon, and tubulin beta chain persisted only within the *Mr*NV-infection group whilst the protein expression in the VLP-invasion group reverted to baseline levels over time, underscoring the transient nature of VLP effects due to their inability to replicate. Additionally, a reduction in peroxiredoxin levels was observed in the later stages of *Mr*NV infection, indicating a potential viral strategy to trigger apoptosis and release virions. Our results suggest that *Mr*NV increases expression of 40S ribosome activity to boost viral protein synthesis while suppressing 60S ribosome expression, which impedes the synthesis of host proteins. *Mr*NV also appears to extend the lifespan of host cells by interfering with their cell cycle and blocking apoptotic pathways, thus facilitating viral replication. This research enhances our comprehension of *Mr*NV's infectious mechanism, delineates the pathways exploited by the virus, and identifies crucial molecular targets for potential therapeutic intervention.

## 1. Introduction

The giant freshwater prawn, *Macrobrachium rosenbergii*, is a vital aquaculture resource. As of 2021, the prawn production reached 327,828 t (Food and Agriculture, 2021). A notable challenge that reduces the prawn production is the prevalence of white tail disease (WTD) caused by *Macrobrachium rosenbergii* nodavirus (*Mr*NV), which is a pervasive threat worldwide (Chen et al., 2021). Initially detected in Guadeloupe in 1997 (Arcier et al., 1999), *Mr*NV has emerged as a transboundary viral pathogen, spreading across various regions, often resulting in 100 % mortality in post-larvae. Presently, effective treatments for WTD are lacking, while efforts to develop prophylaxis against WTD are ongoing (Chen et al., 2023), but both are not ready for commercial applications. A limiting factor to this translational research is a

* Corresponding author.
*E-mail address:* ronald.lee@monash.edu (R.F.S. Lee).

https://doi.org/10.1016/j.aquaculture.2024.741915
Received 3 April 2024; Received in revised form 9 October 2024; Accepted 17 November 2024
Available online 21 November 2024

lack of understanding of *Mr*NV's infection mechanism.

In recent years, efforts have been made to study the mechanism of *Mr*NV infection. Significant molecular processes governing *Mr*NV trafficking, such as its binding and entry into host cells, the formation and subsequent escape from endosomes, and its migration towards the host nucleus for replication, have been examined (Goh et al., 2014; Hanapi et al., 2017; Sirikharin et al., 2019; Somrit et al., 2016). Studies have revealed that the protruding domain of the *Mr*NV capsid protein interacts with transglutaminase and employs the caveolin-mediated pathway for cell entry. Upon encapsulation, *Mr*NV traverses the cytoplasm towards the nucleus, potentially utilising the endosomal acidification process to destabilize the endosomal membrane before escaping the organelle. The presence of a nuclear localization signal on the viral capsid protein facilitates *Mr*NV migration to the nucleus (Hanapi et al., 2017). Interestingly, while nuclear entry may not be necessary for the viral replication, it is theorised that *Mr*NV modulates nucleocytoplasmic trafficking, resulting in the excessive migration of nuclear proteins into the cytoplasm (Flather and Semler, 2015). This alteration permits *Mr*NV to conduct viral replication proximal to the nucleus and endoplasmic reticulum.

Generally, viral infections often induce alterations in the host cell's physiological processes to manipulate its protein production machinery, facilitating the synthesis of viral proteins (Wang et al., 2007). Viruses have evolved sophisticated strategies to manipulate cellular pathways, including the cell cycle, apoptosis, and antiviral responses, aiming to enhance viral RNA transcriptions while hindering host cellular mechanisms to prevent premature viral clearance (Barber, 2001). In this regard, Pasookhush et al. (2019) employed transcriptomics to investigate the impact of *Mr*NV infection and observed significant changes in the mRNA expression of immune response proteins, phagocytosis, apoptosis, and RNA interference in infected post-larvae. Upregulation of mRNAs encoding the pattern recognition proteins like the C-type lectin and mannose-binding lectin suggests their potential role in combating *Mr*NV infection. Conversely, downregulation of mRNA associated with the toll immune deficiency (IMD) signalling pathways, such as the spätzle protein, implies a reduction in antimicrobial peptide production. Additionally, upregulation of mRNAs encoding several caspases and inhibitors of apoptosis proteins indicates that *Mr*NV could inhibit apoptosis. However, it should be noted that transcriptomic data may not directly correlate with changes in protein levels due to factors such as rapid degradation or inefficient translation of mRNA into proteins (Hanson and Coller, 2017; Neymotin et al., 2016). Furthermore, transcriptomic studies often overlook crucial post-translational modifications on proteins that play a pivotal role in their functionality (Gunawardana and Niranjan, 2013; Takemon et al., 2021). Therefore, conducting proteomic studies is imperative to comprehend the alterations in protein levels induced by infections. Despite the importance of such investigations, there is a notable absence of such studies examining the effects of *Mr*NV infection in both *in vitro* and *in vivo* models. This scarcity may stem from challenges such as the limited availability of proteins in databases related to the host organisms of *Mr*NV. Therefore, in the present study, we aimed to conduct proteomic analysis on *Mr*NV-infected *Sf9* cells throughout early to late-stage infection, aiming to elucidate time-resolved differential protein expression changes in response to infection. *Sf9* cells derived from *Spodoptera frugiperda* serve as a valuable model for studying *Mr*NV infection due to their susceptibility to *Mr*NV infection and the virus propagates efficiently within these cells (Somrit et al., 2016). To the best of our knowledge, this is the first study to understand the mechanism of MrNV infection across its early to late-stage progression by employing a proteomic approach.

## 2. Materials and methods

### 2.1. Expression and purification of MrNV-VLP from E. coli

*E. coli* cells containing the recombinant plasmid encoding the *Mr*NV capsid protein (Goh et al., 2011) were cultured on Luria Broth (LB) agar supplemented with ampicillin (50 μg/ml), and incubated overnight at 37 °C. A single bacterial colony of the overnight culture was then inoculated into 500 ml of LB broth containing ampicillin (50 μg/ml), and then incubated in a shaking incubator (37 °C, 220 rpm). The optical density of the culture at wavelength 600 nm ($OD_{600}$) was recorded until it reached 0.6–0.8. Subsequently, 500 μl of 1 M isopropyl β-d-1-thiogalactopyranoside (IPTG) was added to induce the capsid protein expression, followed by further incubation at room temperature for 5 h (220 rpm) before centrifugation at 5400 ×*g* for 10 min (4 °C) to pellet the cells. The cell pellets were resuspended in 15 ml of lysis buffer [25 mM 4-(2-hydroxyethyl)-1-piperazineethanesulfonic acid (HEPES), 500 mM NaCl; pH 7.4] containing 4 mM $MgCl_2$ and 0.2 mg/ml freshly prepared lysozyme. After gentle mixing, 2 mM phenylmethylsulfonyl fluoride (PMSF) and 0.02 mg/ml DNase I were added to the cell culture, followed by incubation at room temperature for 2 h. The mixture was then sonicated using a probe sonicator at 200 Hz for 20 s for 10 cycles to lyse the cells. After sonication, the mixture was centrifuged at 12,000 ×*g* for 10 min (4 °C), and the supernatant was filtered using a 0.45 μm cellulose acetate pore filter before loading onto a calibrated His-Trap HP 5 ml column (GE Healthcare, Buckinghamshire, United Kingdom). The bound sample was washed sequentially with binding buffer A (25 mM HEPES, 500 mM NaCl, 50 mM imidazole, pH 7.4) and binding buffer B (25 mM HEPES, 500 mM NaCl, 200 mM imidazole, pH 7.4), followed by elution with elution buffer (25 mM HEPES, 500 mM NaCl, 500 mM imidazole, pH 7.4). The eluted samples containing *Mr*NV VLPs were pooled and dialysed against HEPES buffer (25 mM HEPES, 150 mM NaCl; pH 7.4) for 2 h, followed by buffer exchange with fresh HEPES buffer and overnight dialysis.

### 2.2. SDS-PAGE and determination of protein concentration

The eluted samples (10 μl) from the above His-Trap HP column filtration were combined with 10 μl of SDS sample buffer [100 mM Tris–HCl; pH 6.8, 20 % glycerol (v/v), 4 % SDS (w/v), 0.2 % (w/v) bromophenol blue, 200 mM mercaptoethanol], and incubated on a heat block at 95 °C for 5 min. Following incubation, the samples were centrifuged at 16,000 ×*g* for 5 min. Subsequently, they were loaded onto SDS-polyacrylamide [12 % (w/v)] gels, and electrophoresed at 100 V until the dye migrated to the end of the gel. Following electrophoresis, the gels were stained with Coomassie Brilliant Blue R-250 (Sigma-Aldrich, Missouri, USA) for 20 min, and destained with destaining solution [30 % (v/v) ethanol and 10 % (v/v) glacial acetic acid].

The concentration of dialysed *Mr*NV VLPs was determined with the Bradford assay (Bradford, 1976) using bovine serum albumin (BSA) as the standard.

### 2.3. Confirmation of natural propagation of MrNV in M. rosenbergii postlarvae and Sf9 cells via reverse transcription (RT)-PCR

*Mr*NV-infected postlarvae (PL) exhibited prominent signs of whitish muscle in the abdominal region (a gift from Dr. Kok Lian Ho from Universiti Putra Malaysia) served as the source of wildtype *Mr*NV. The frozen infected PL (100 mg) were thawed in 1 ml of Trizol to yield a 10 % (*v*) suspension. Homogenization was performed using a pestle homogenizer, and the mixture was incubated at room temperature for 5 min before adding 0.2 ml of chloroform. After vigorous shaking for 15 s, the mixture was left for 15 min at room temperature. Subsequently, the mixture was centrifuged at 12,000 ×*g* at 4 °C for 15 min, and the aqueous layer was carefully transferred into a fresh microcentrifuge tube. Addition of 0.5 ml of isopropanol (100 % v/v) followed by a 10-min incubation at room temperature facilitated RNA precipitation. The mixture was then centrifuged at 12,000 ×*g* at 4 °C for 10 min to pellet the RNA, after which the supernatant was discarded. The RNA pellet was washed with 1 ml of 75 % (v/v) ethanol via vortexing and centrifuged at 12,000 ×*g* at 4 °C for 5 min. After aspirating the ethanol,

the pellet was air-dried, and subsequently resuspended in 50 μl of ultrapure DNase/RNase-free water at 55 °C for 10 min.

RNA concentration and yield were determined using a NanoDrop spectrophotometer (Thermo Fisher Scientific, Massachusetts, USA). cDNA synthesis was performed utilising an iScript cDNA synthesis kit (Bio-Rad Laboratories, California, USA). The presence of *Mr*NV was confirmed using the $RNA1_{1–205}$ forward (5′-GTTAAACGTTTTGTTTTC-TAGC-3′) and reverse (5′-TAAGGTCCGATTACCACATA-3′) primers for *Mr*NV RNA1 (Jariyapong et al., 2018). The amplified PCR products (205 bp) were purified using a PCR purification kit (Qiagen, Germany) before DNA sequencing. Gel electrophoresis was employed to assess the size of the amplified PCR products. Pairwise sequence analysis was conducted using the Basic Local Alignment Search Tool (BLAST) program (http://www.ncbi.nlm.nih.gov/BLAST) available through the National Centre for Biotechnology Information (NCBI).

### 2.4. Cell culture and treatment

*Sf*9 cells (ATCC® CRL-1711™) were initially seeded into a 75 $cm^2$-cell culture flask containing 10 % fetal bovine serum (FBS) (Thermo Fisher Scientific, Massachusetts, USA) in Sf900 III SFM medium (GIBCO, Grand Island, NY, USA), and maintained at 27 °*C. media* exchange was carried out every three days with fresh media to sustain cell viability. Upon reaching approximately 90 % confluence, the cells were sub-cultured into new flasks. This process was repeated for three passages to ensure the stability of the cell culture before any experimental studies were conducted.

### 2.5. Production of viral inocula

*Macrobrachium rosenbergii* PL with confirmed *Mr*NV infection were homogenised using a sterile pestle homogeniser to obtain a crude protein extract. The *Mr*NV inoculum was prepared using the method outlined by Somrit et al. (2016). In brief, a suspension of PL in buffer was made using 1 ml of phosphate-buffered saline (PBS: 137 mM NaCl, 2.7 mM KCl, 10 mM $Na_2HPO_4$, 2 mM $KH_2PO_4$) for every 100 mg of PL. The homogenized suspension was centrifuged (400 ×*g*, 4 °C, 10 min) and the supernatant was recovered. This was followed with another round of centrifugation (12,000 ×*g*, 4 °C, 30 min). The supernatant was filtered through a 0.22 μm pore cellulose acetate membrane, and the concentration of the crude protein extract was determined using a NanoDrop spectrophotometer.

*Sf*9 cells were seeded onto 6-well plates at a cell density of $2 \times 10^6$ cells/well, and cultured for 24 h at 27 °C. Subsequently, the cells were pre-chilled at 4 °C, and the *Mr*NV inoculum was added to the medium at a final concentration of 40 μg/ml, with continuous gentle shaking. Following incubation (4 °C, 1 h), the excess *Mr*NV inoculum solution was removed, replaced with fresh medium, and incubated for three days.

Media were harvested and filtered through a 0.22 μm pore membrane. The freshly harvested *Mr*NV filtrate was designated as passage 0 (P0). Newly sub-cultured *Sf*9 cells in a 75 $cm^2$ flask were pre-chilled at 4 °C before the addition of *Mr*NV filtrate from P0. After incubation (4 °C, 1 h), the excess *Mr*NV inoculum solution was removed, replaced with fresh medium, and incubated for three days. To establish stable *Mr*NV production, reinfection of healthy *Sf*9 cells was conducted using previously harvested *Mr*NV filtrate until passage two was achieved, before finally filtering the filtrate again through a 0.22 μm pore membrane. The resulting filtrate was then stored at −20 °C for experimental infection.

### 2.6. Infection assay

The infectivity assay encompassed three conditions (untreated controls, *Mr*NV VLP invasion, and *Mr*NV infection) conducted at three distinct time points (30 min, 2 h, and 24 h). *Mr*NV VLP (from Section 2.1) and *Mr*NV viral inocula (from Section 2.5) served as the sources of infection. *Sf*9 cells ($1.5 \times 10^6$ cells/well) were seeded into each well of a 6-well culture plate and cultured for 24 h. Subsequently, the cells were pre-chilled at 4 °C before the addition of the inoculum containing *Mr*NV VLP (25 μg) or *Mr*NV extract [10 % (v/v)]. After incubation (4 °C, 1 h), excess *Mr*NV VLP or *Mr*NV was removed, and fresh media were added, followed by incubation at 27 °C. The morphology of the *Sf*9 cells was observed under an inverted microscope at 20× magnification (Olympus CKX53, Tokyo, Japan).

Throughout the harvesting process, both the cells and solutions were maintained on ice. The *Sf*9 cells were transferred into microcentrifuge tubes and centrifuged (500 ×*g*, 4 °C) for 10 min. The media were aspirated, and the pellet was washed with 500 μl ice-cold PBS. After centrifugation (500 ×*g*, 4 °C) for 10 min, the supernatant was removed. The pellet was resuspended in 200 μl of Radio-Immunoprecipitation Assay (RIPA) buffer [150 mM NaCl, 50 mM Tris-HCl pH 8.0, 1 % (v/v) Nonidet P-40, 0.5 % sodium deoxycholate, 0.1 % SDS] supplemented with 1× protease and phosphatase inhibitors. The mixture was further homogenised using a pestle homogeniser until the solution became cloudy. After centrifugation (500 ×*g*, 4 °C) for 5 min, the supernatant was collected and stored at −20 °C for subsequent processing.

### 2.7. Liquid chromatography with tandem mass spectrometry (LC-MS/MS) sample processing and data analysis

#### 2.7.1. In-solution tryptic digestion

The protein concentration in each sample was determined using the Bradford assay (Bradford, 1976). Specifically, 0.2 mg of protein extracted from previously lysed cells was carefully transferred into new low-protein binding microcentrifuge tubes. Subsequently, 25 μl of 100 mM ammonium bicarbonate and 25 μl of trifluoroethanol, serving as a denaturation agent, were added to each sample. To facilitate protein reduction, 1 μl of 200 mM dithiothreitol (DTT) was introduced before heating the samples at 60 °C for 1 h. After allowing the samples to cool, alkylation was performed by adding 4 μl of 200 mM iodoacetamide (IAM) to each sample, followed by incubation at room temperature in the dark for 1 h. To quench any excess IAM, 1 μl of DTT was added, and incubated for an additional hour in the dark at room temperature. The sample was diluted with 300 μl of ultrapure water, followed by the addition of 100 μl of 100 mM ammonium bicarbonate. Trypsin solution (1 μg/μl) was added into the sample at a ratio of 1:20 (mass of enzyme to substrate) to initiate protein digestion. The tubes were then incubated at 37 °C for 18 h. After cooling, trypsin activity was halted by adding 1 μl of formic acid (FA) to the samples. Finally, the samples were dried overnight in a centrifugal evaporator.

#### 2.7.2. Sample clean-up

The dried samples were resuspended in 30 μl of 0.5 % (v/v) trifluoroacetic acid (TFA) and 5 % (v/v) acetonitrile (ACN) in water. Subsequently, 10 μl of sample buffer [2 % (v/v) TFA and 20 % (v/v) ACN in water] was added to each sample. Pierce C18 Spin Columns (Thermo Fisher Scientific, Massachusetts, USA) were prepared by tapping to settle the resin, followed by the removal of caps from both ends of the tube. The columns were then positioned in a receiver tube, and 200 μl of activation solution (50 % (v/v) methanol) was employed to activate the resin, followed by centrifugation at 1500 ×*g* for 1 min. This activation step was repeated once more, with the flow-through being discarded each time. Equilibration of the columns was accomplished by adding 200 μl of equilibrium solution [0.5 % (v/v) TFA in 5 % (v/v) ACN] to each tube before centrifugation, the flow-through was discarded, and the equilibrium step was repeated. The sample was loaded onto the top of the resin bed, and the spin columns were transferred to a low protein binding microcentrifuge tube for centrifugation. The flow-through was collected, reloaded onto the resin bed to ensure complete sample binding, and centrifuged once more before retention and storage at −20 °C. The spin columns were then transferred back to the original receiver tube. Subsequent washing steps involved the addition of 200 μl of wash

solution [0.5 % (v/v) TFA in 5 % (v/v) ACN to the columns before centrifugation, and the flow-through was discarded. This washing process was repeated three times to ensure thorough removal of contaminants. The spin columns were then transferred to a new low-protein binding microcentrifuge tube. For elution, 20 μl of elution buffer [70 % (v/v) ACN] was loaded onto the top of the resin bed and centrifuged. This elution step was repeated into the same low-protein binding microcentrifuge tube. The purified samples were subsequently dried overnight in a vacuum evaporator before storage at −20 °C prior to LC/MS analysis.

#### 2.7.3. Nanoflow liquid chromatography electrospray-ionisation coupled with tandem mass spectrometry (Nanoflow–ESI–LC–MS/MS)

Nanoflow–ESI–LC–MS/MS protocol employed was as described by Zainal Abidin et al. (2016). In brief, the digested peptides were injected into an Agilent C18 300 Å Large Capacity Chip (Agilent, Santa Clara, CA, USA) column that had been pre-equilibrated with 0.1 % (v/v) formic acid in water (solution A). Peptide elution was performed using a gradient of 90 % (v/v) acetonitrile (ACN) in 0.1 % (v/v) formic acid in water (solution B), with the following gradient profile: 3 %–50 % solution B over 0–30 min, 50 %–95 % solution B over 2 min, maintaining 95 % solution B for 7 min, and finally transitioning to 3 % solution B over 39–47 min. For Quadrupole-time of flight (Q-TOF) analysis, the polarity was set to positive mode, with capillary and fragmenter voltages at 2050 V and 300 V, respectively, and a gas flow rate of 5 l/min at 300 °C. Peptide spectra were acquired in auto MS mode, covering a mass range of 110–3000 *m/z* for MS scans and 50–3000 m/z for MS/MS.

#### 2.7.4. Bioinformatics

The peptide spectrum acquired was analysed using Agilent MassHunter data acquisition software and PEAKS 7.0 software (Bioinformatics Solutions Inc. Waterloo, ON, Canada). This involved matching the peptide sequences with the NCBI nr database to identify the proteins present. During the matching of protein sequences, the *Sf9* database was used as reference whenever possible. However, closely related species such as *Spodoptera exigua* and *Spodoptera litura* was referenced when the peptides were not detectable within the *Sf9* database. Further processing of identified proteins was conducted to procure functional annotations for each differentially expressed protein. Gene ontology (GO) was used to annotate gene functions, locations, and biological roles of proteins (Ashburner et al., 2000; The Gene Ontology Consortium, 2023). To extract the GO information from each of our proteins, we utilised Blast2GO, a bioinformatics tool within OmicsBox (BioBam Bioinformatics, Valencia, Spain), which employs NCBI BLAST to match protein sequences against the NCBI nr database. The annotations were then categorised into their own ontology group: biological processes, molecular function, and cellular component. Pathway analysis was performed in OmicsBox using two pathway databases i.e. the Kyoto Encyclopedia of Genes and Genomes (KEGG) database and the Reactome database (Kanehisa and Goto, 2000; Fabregat et al., 2017) Pathways detected by Reactome were subjected to an overrepresentation analysis to determine the significance of the pathways detected.

## 3. Results

### 3.1. Expression of MrNV-VLP from E. coli cell culture

SDS-PAGE analysis of the purified *Mr*NV capsid protein gave rise to a distinct band of ~46 kDa (see supplementary material Fig. S1). The molecular mass of the recombinant protein corresponded well with that reported by Goh et al. (2011) and Hanapi et al. (2017). The yield of the purified recombinant protein was ~980 mg from a 1000 ml culture.

### 3.2. Confirmation of naturally MrNV-infected M. rosenbergii post-larvae

RNA extracted from homogenized *Mr*NV-infected *M. rosenbergii* post-larvae, and *Sf9* cells were reversed transcribed to cDNA. In order to detect the presence of *Mr*NV, amplification of RNA1 using the primers RNA1-F/$R_{1-205}$ was performed, which produced an expected band size of 205 bp on an agarose gel (see supplementary material Fig. S2). Amplification of *Mr*NV cDNA derived from *Sf9* cells also produced a band of 205 bp. DNA sequencing of the amplicons from the post-larvae and *Sf9* cells showed an identity score of 98.25 % and 98.65 %, respectively, as compared with the specified segment from GenBank Acc. No. AY222839.1. This confirmed the presence of *Mr*NV in post-larvae, and the ability of the virus to propagate in *Sf9* across multiple passages.

### 3.3. Morphology of MrNV-infected Sf9 cells at different time points

The morphologies of *Mr*NV VLP-invaded and *Mr*NV-infected *Sf*9 cells were compared with a control group at four different time points (30-min, 60-min, 120-min, and 24-h). The *Mr*NV VLP-invaded *Sf*9 cells (Fig. 1a) displayed a regular cell size, shape, and smooth outer membrane similar to the healthy *Sf*9 cells (Fig. 1b) for all time points. For the *Mr*NV-infected group, no changes were detected within the first 30 min (Fig. 1c). At 60-min *Mr*NV-infected *Sf*9 cells exhibited mild cytopathic effect, with cells showing irregularity along their cell membrane (Fig. 1f). At 120 min, the cytopathic effect in *Mr*NV-infected *Sf*9 cells

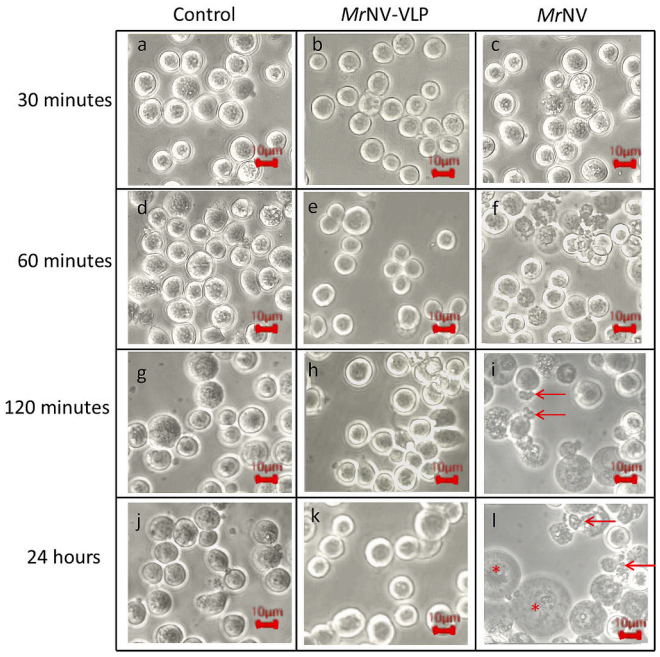


**Fig. 1.** Timepoint infectivity assay of *Mr*NV VLP invasion and *Mr*NV infection on *Sf9* cells. The cells were viewed under an Olympus CKX53 inverted microscope at 20× magnification. After 30 min of incubation, *Sf*9 cells incubated with MrNV VLP (b) and *Mr*NV (c) had no changes in morphology when compared to the control group (a). At this time point, no significant changes were observed in the morphology and cell size of these three samples. At the 60-min time point (d, e, f), *Mr*NV-infected *Sf*9 cells exhibited irregularity along their cell membrane. At 120-min, *Sf*9 cells invaded with *Mr*NV VLP (h) showed no difference in morphology compared to the control group (g). However, a proportion of *Mr*NV-infected *Sf*9 cells (i) exhibited an increase in cell size, with most cells displaying mild disruption (red arrow). After 24 h, the control group (j) and *Mr*NV VLP-invaded *Sf*9 cells (k) showed no sign of cytopathic effect. However, for *Mr*NV-infected *Sf*9 cells (l), the cells displayed mild to severe cytopathic effect, including slight disruption of the cell membrane, increased granularity, and vacuolation (red asterisk). A proportion of the cells grew to approximately twice the size of normal *Sf*9 cells, while a proportion of *Sf*9 cells displayed disproportionate and shrunken sizes. (For interpretation of the references to colour in this figure legend, the reader is referred to the web version of this article.)

had increased in severity, with some cells showing an irregular shape and a decrease in size, whilst the other cells showed an increase in size (Fig. 1i). At 24 h, most *Sf*9 cells showed severe cytopathic effects (Fig. 1l), with the average cell size doubling compared to the control group. Many of the enlarged cells exhibited increased granularity and vacuolation, while a proportion of cells shrank below the standard cell size, exhibiting a highly disproportionate cell membrane structure.

### 3.4. Identification of differentially expressed proteins among control and infected Sf9 cells at 30 min, 120 min, and 24 h post-infection

The peptides detected from the samples were searched against the *Sf9* protein database as well as *S. exigua* and *S. litura* (if the protein was not found within the *Sf9* database). LC-MS/MS proteomics was used to study differential protein expression during various stages of *Mr*NV infection in *Sf*9 cells. The heatmap (Fig. 2) shows the relative expression difference for proteins detected commonly across all 3 treatment groups, i.e, untreated controls, *Mr*NV VLP-invaded and *Mr*NV-infected *Sf*9 cells. Expression levels were normalized to that of controls. Relative expression differences are also provided in numerical format in Table 1.

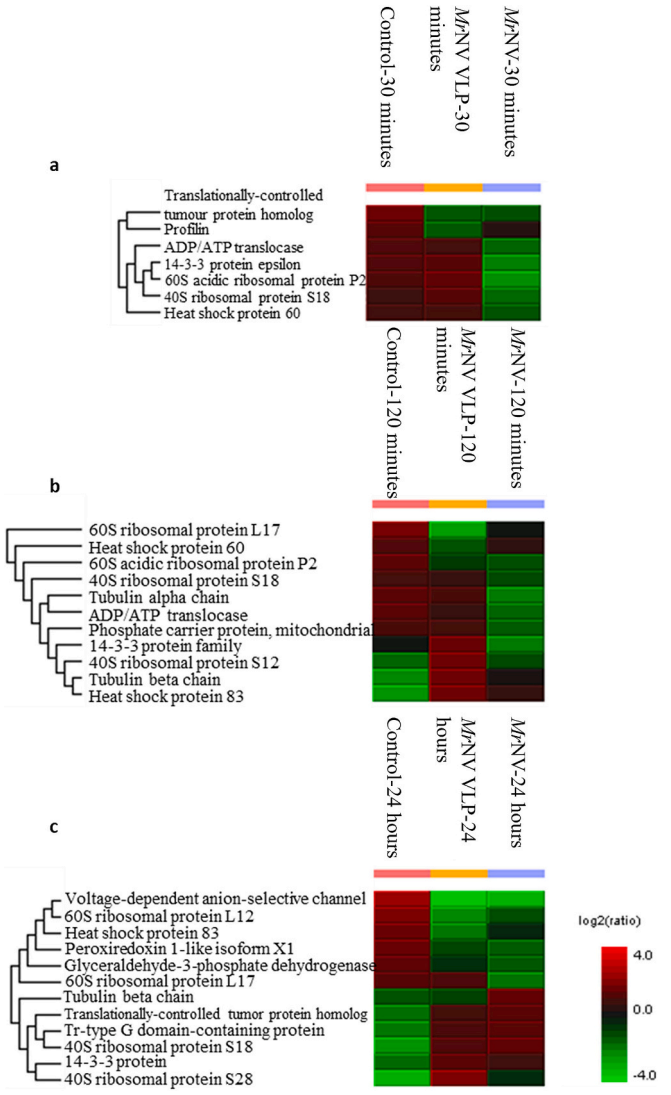


**Fig. 2.** Heatmap of the differentially expressed proteins when compared between control, *Mr*NV VLP-invaded, and *Mr*NV-infected *Sf9* cells. Each heatmap represents a different timepoint with (a) 30 min and (b) 120 min showing early to early-mid stage infection, and (c) 24 h showing the effects of late-stage *Mr*NV infection in *Sf9* cells. The protein expression levels are compared in terms of their relative expression. *Mr*NV VLP-invaded and *Mr*NV-infected groups are compared against the control *Sf9* group, with the relative expression of the control group set to 1.00 by default.

### 3.5. Gene ontology annotations

The BLAST analysis and functional annotation extraction yielded 179 annotation terms associated with the GO biological process, cellular component, and molecular function categories (Fig. 3). Predominantly, the proteins were implicated in translation, folding, and glycolytic processes within the biological process category. Notably, subcategories such as translational elongation, cytoplasmic translation, maturation of SSU-rRNA, ncRNA processing, and ribosome biogenesis were frequently observed. Regarding the cellular component category, the proteins were predominantly associated with the cytoplasm, ribonucleoprotein complex, and components related to ribosomes. Most identified proteins played integral roles in translation processes within the endoplasmic reticulum. In the molecular function category, a majority of the proteins were linked to the structural constituent of ribosomes, translation activity, binding of unfolded proteins, and various catalytic activities including ATP-binding and hydrolysis, GTP binding and GTPase activity, and NAD/NADP binding.

### 3.6. Pathway enrichment analysis

We employed OmicsBox to conduct a combined pathway enrichment analysis, leveraging the KEGG and Reactome databases using previously identified GO terms. We utilized both KEGG and Reactome due to their complementary analyses of protein pathways (Mubeen et al., 2019). KEGG pathways offer comprehensive mappings of biochemical relationships across a diverse array of organisms. Conversely, Reactome is distinguished by its meticulous manual curation by experts, providing an overview of pathways and detailed subsections within each biological process and molecular events, sourced from primary literature. As a result, KEGG pathways afford a broad and systematic overview, while Reactome furnishes intricate molecular insights, with some pathways overlapping between the two databases. Furthermore, we conducted an overrepresentation analysis using the Reactome bioinformatics tool, enabling us to identify significant pathways associated with the proteins we identified.

### 3.7. KEGG pathway analysis

Every cellular function and biochemical reaction involve different protein pathways which are archived in the KEGG pathway database. We utilised OmicsBox, to align identified pathways in the KEGG database with insect proteins and their associated pathways. One notable protein detected from our analysis was heat shock protein 83 (Hsp83, also known as heat shock protein 90). Among its many roles during a stress response is its involvement in the PI3K-AKT signalling pathway (Fig. 4). An elevation in Hsp83 levels was observed during the early stages of infection, enhancing its interaction with protein Akt. This interaction leads to the phosphorylation of tuberous sclerosis complex 2 (TSC2), thereby disrupting the complex formation between TSC2 and tuberous sclerosis complex 1 (TSC1). Consequently, Ras homologue enriched in the brain (Rheb) is relieved from inhibition, activating mTOR. This activation further promotes the phosphorylation of S6K and 4EBP1 proteins, facilitating the translation of viral mRNAs. Additionally, an ancillary pathway involves the regulation of the cell cycle and apoptosis mediated by 14–3-3 protein epsilon. Furthermore, several other proteins displayed significant up- and down-regulation, including the 40S and 60S ribosomal subunits, impacting protein translation (Fig. 5).

**Table 1**
A list of differentially expressed proteins categorised by the type of proteins and the relative expression levels from each *Sf9* group at each time point.

| Protein | Sample group | Expression at 30 min (Ratio) | Expression at 120 min (Ratio) | Expression at 24 h (Ratio) |
|---|---|---|---|---|
| 60S ribosomal subunit L12 | *Sf9* Control | 1.00 | 1.00 | 1.00 |
| | *Mr*NV-VLP-*Sf9* | 1.00 | 1.00 | 0.49 |
| | *Mr*NV-Sf9 | 1.00 | 1.00 | 0.40 |
| 60S ribosomal subunit L17 | *Sf9* Control | 1.00 | 1.00 | 1.00 |
| | *Mr*NV-VLP-*Sf9* | 1.00 | 0.13 | 0.92 |
| | *Mr*NV-Sf9 | 1.00 | 0.57 | 0.37 |
| 40S ribosomal subunit S12 | *Sf9* Control | 1.00 | 1.00 | 1.00 |
| | *Mr*NV-VLP-*Sf9* | 1.00 | 2.78 | 1.00 |
| | *Mr*NV-Sf9 | 1.00 | 1.32 | 1.00 |
| 40S ribosomal subunit S18 | *Sf9* Control | 1.00 | 1.00 | 1.00 |
| | *Mr*NV-VLP-*Sf9* | 1.00 | 0.91 | 4.28 |
| | *Mr*NV-Sf9 | 1.00 | 0.67 | 4.83 |
| 40S ribosomal subunit S28 | *Sf9* Control | 1.00 | 1.00 | 1.00 |
| | *Mr*NV-VLP-*Sf9* | 1.00 | 1.00 | 13.23 |
| | *Mr*NV-Sf9 | 1.00 | 1.00 | 6.58 |
| Heat shock protein 83 | *Sf9* Control | 1.00 | 1.00 | 1.00 |
| | *Mr*NV-VLP-*Sf9* | 1.00 | 5.54 | 0.30 |
| | *Mr*NV-Sf9 | 1.00 | 3.54 | 0.62 |
| 14–3-3 protein epsilon | *Sf9* Control | 1.00 | 1.00 | 1.00 |
| | *Mr*NV-VLP-*Sf9* | 1.00 | 1.55 | 2.47 |
| | *Mr*NV-Sf9 | 1.00 | 0.45 | 2.04 |
| GADPH | *Sf9* Control | 1.00 | 1.00 | 1.00 |
| | *Mr*NV-VLP-*Sf9* | 1.00 | 1.00 | 0.67 |
| | *Mr*NV-Sf9 | 1.00 | 1.00 | 0.48 |
| Peroxiredoxin 1-like isoform X1 | *Sf9* Control | 1.00 | 1.00 | 1.00 |
| | *Mr*NV-VLP-*Sf9* | 1.00 | 1.00 | 0.52 |
| | *Mr*NV-Sf9 | 1.00 | 1.00 | 0.42 |
| Tubulin beta chain | *Sf9* Control | 1.00 | 1.00 | 1.00 |
| | *Mr*NV-VLP-*Sf9* | 1.00 | 4.52 | 1.17 |
| | *Mr*NV-Sf9 | 1.00 | 2.77 | 2.05 |
| Tr-Type G domain-containing protein | *Sf9* Control | 1.00 | 1.00 | 1.00 |
| | *Mr*NV-VLP-*Sf9* | 1.00 | 1.00 | 2.64 |
| | *Mr*NV-Sf9 | 1.00 | 1.00 | 2.93 |
| Translationally-controlled tumour protein (TCTP) | *Sf9* Control | 1.00 | 1.00 | 1.00 |
| | *Mr*NV-VLP-*Sf9* | 1.00 | 1.00 | 2.21 |
| | *Mr*NV-Sf9 | 1.00 | 1.00 | 2.56 |

### 3.8. Reactome pathway analysis

Reactome serves as a robust bioinformatics tool, facilitating the visualization, interpretation, and analysis of pathways (Fabregat et al., 2017). We enriched our set of differentially expressed proteins (DEPs) using Reactome's meticulously curated database of pathways and reactions, initially matching towards the *Drosophila melanogaster* database before validating the pathway on a human database. Employing an overrepresentation analysis, we determined the probability score of each relevant pathway enriched by our dataset, subsequently correcting for false discovery rate (FDR) using the Benjamini-Hochberg method.

Upon application of our dataset to the database, we obtained a comprehensive list of all possible pathway interactions, each with calculated FDR values indicating the significance of a given pathway (Table 2). Notable proteins within the metabolism of proteins and RNA pathways, including 40S ribosomal protein S18 and S28, and 60S ribosomal protein L12 and L17, were identified. These proteins play pivotal roles in eukaryotic translation elongation and termination, formation of free 40S subunits, L13a-mediated translational silencing of Ceruloplasmin expression, GTP hydrolysis and joining of the 60S ribosomal subunit, and ribosomal scanning and start codon recognition, all integral parts of the eukaryotic translation initiation pathway. Additionally, viral infection-related pathways, such as viral mRNA translation, influenza infection, and viral infection pathways, were flagged, underscoring the dependence of viral replication on the host cell's energy reserves. Pathways such as cellular response to starvation and RHOBTB2 GTPase cycle were also highlighted in this context.

Furthermore, 14–3-3 protein epsilon, a conserved regulatory protein, was implicated in pathways affecting cell proliferation, cell cycle regulation, actin cytoskeleton regulation, and the mTOR pathway (Fig. 6). This suggests significant perturbations in the host mitotic cell cycle due to *Mr*NV infection. All pathways discussed herein underwent stringent screening to ensure their FDR values were equal to or less than 5 %, thus confirming their significant involvement in *Mr*NV infection. Moreover, a protein exhibiting the molecular function of peroxiredoxin activity displayed decreased expression levels during the late stages of infection. Referred to as peroxiredoxin 1-like isoform X1, this protein plays a vital role in cellular responses to oxidative stress by detoxifying reactive oxygen species. Additionally, 14–3-3 protein epsilon was implicated in various cellular pathways, including cell proliferation, cell cycle regulation, actin cytoskeleton regulation, and the mTOR pathway (Fig. 6).

## 4. Discussion

In order to understand the protein change pathways implicated in the mechanism of infection of *Mr*NV, we performed expression proteomics to identify proteins that had significantly changed between healthy, *Mr*NV VLP-invaded, and *Mr*NV-infected *Sf9* cells. To our knowledge, this is the first study examining time resolved morphological and protein expression changes between normal, *Mr*NV VLP-invaded, and *Mr*NV-infected *Sf9* cells. We utilised the *Sf*9 model for our study as (1) it is a known host for *Mr*NV infection, (2) ease of maintenance and lower proteome variability from being an immortalized cell line, and (3) it has a proteome database that is reasonably well characterized. To augment the proteomic analysis, we also compared the detected proteins horizontally and vertically within the taxonomy tree, drawing evidence from previous publications. Our findings indicate that the main pathways affected are the mitotic prometaphase (R-DME-68877.1), G2/M transition phases (R-DME-453274.1), eukaryotic translation initiation pathway (R-DME-72613.1) (comprising most of its ancillary pathways), PI3K-Akt signalling pathway, RAB GEFs exchange GTP for GDP on RABs (R-DME-8876198.1), and hydrogen peroxide regulation ($H_2O_2$) pathway.

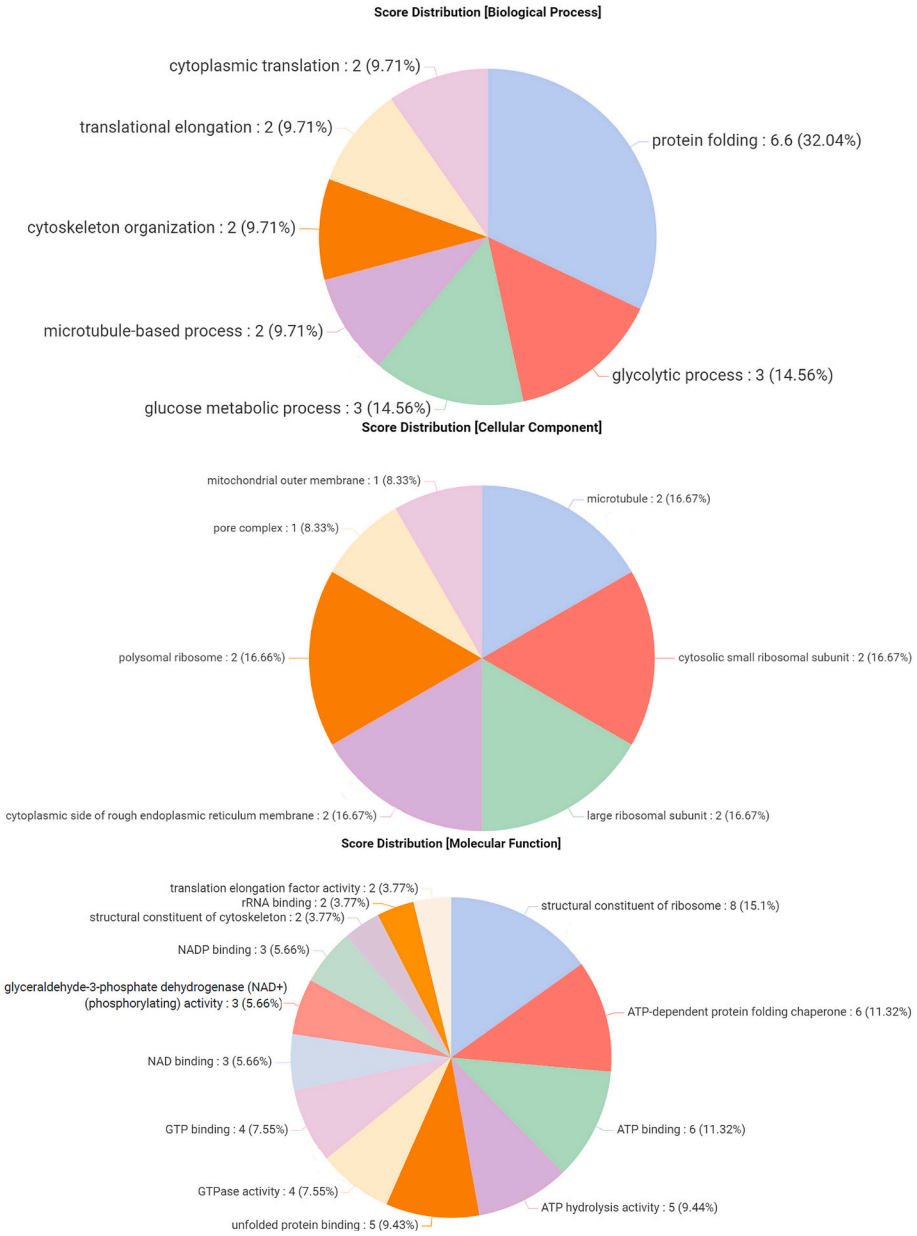


**Fig. 3.** The distribution of GO terms among differentially expressed proteins in *Mr*NV VLP-invaded or *Mr*NV-infected *Sf*9 cells. In terms of biological processes (a), the detected proteins were predominantly associated with cellular and metabolic processes. Subsequently, in terms of cellular components (b), the GO terms were mainly linked to microtubules and ribosomal proteins. Finally, within the molecular function category (c), the majority of proteins were categorised under structural constituents of the ribosome and exhibited functions related to ATP binding and hydrolysis.

### *4.1. Cellular growth and cell cycle arrest*

The cell cycle coordinates the duplication of organelles and genetic information to generate new cells (Israels and Israels, 2000). Progression through this cycle is regulated by cyclin phosphorylation, guiding sequential phases (Rohrmann, 2019). Molecular checkpoints ensure accurate progression, which prevents the replication of damaged cellular components, a process linked to cancer developments. Upon encountering damages, cells halt replication, opting for repair or apoptosis. Viral infections adeptly manipulate the host cell cycle, redirecting replication machinery and thwarting premature apoptosis, facilitating viral proliferation and transmission (Davy and Doorbar, 2007). Our investigation unveiled an upregulation of 14–3-3 protein, notably 14–3-3 epsilon, commencing at 120 min-post-infection. Utilising the KEGG pathways database, we identified the involvement of 14–3-3 epsilon in the AKT/BAD/Bcl-2 signalling pathway, crucial for regulating cell apoptosis (Fig. 4). All 14–3-3 isoforms hinder BAD-induced apoptosis by sequestering BAD in the cytosol, impeding its translocation to mitochondria and subsequent caspase pathway activation (Liou et al., 2006; Subramanian et al., 2001).

As previously noted, the protein 14–3-3 epsilon plays a role in numerous cell cycle pathways identified through Reactome analysis. Within insects, the Hippo signalling pathway and the Hippo/Warts pathway are present, both involving the transcriptional coactivator WW domain-containing transcription regulator protein 1 (WWTR1) and Yorkie (YKI). Activation and increased expression of WWTR1 and YKI stimulate cell proliferation, as their inherent function governs organ sizes and cellular growth (Straßburger et al., 2012; Wang et al., 2014). Reactome analysis has demonstrated that the 14–3-3 epsilon dimers can interact with both transcriptional coactivators in these pathways by binding to phosphorylated WWTR1 and YKI. Consequently, this interaction sequesters both WWTR1 and YKI within the cytosol, thereby

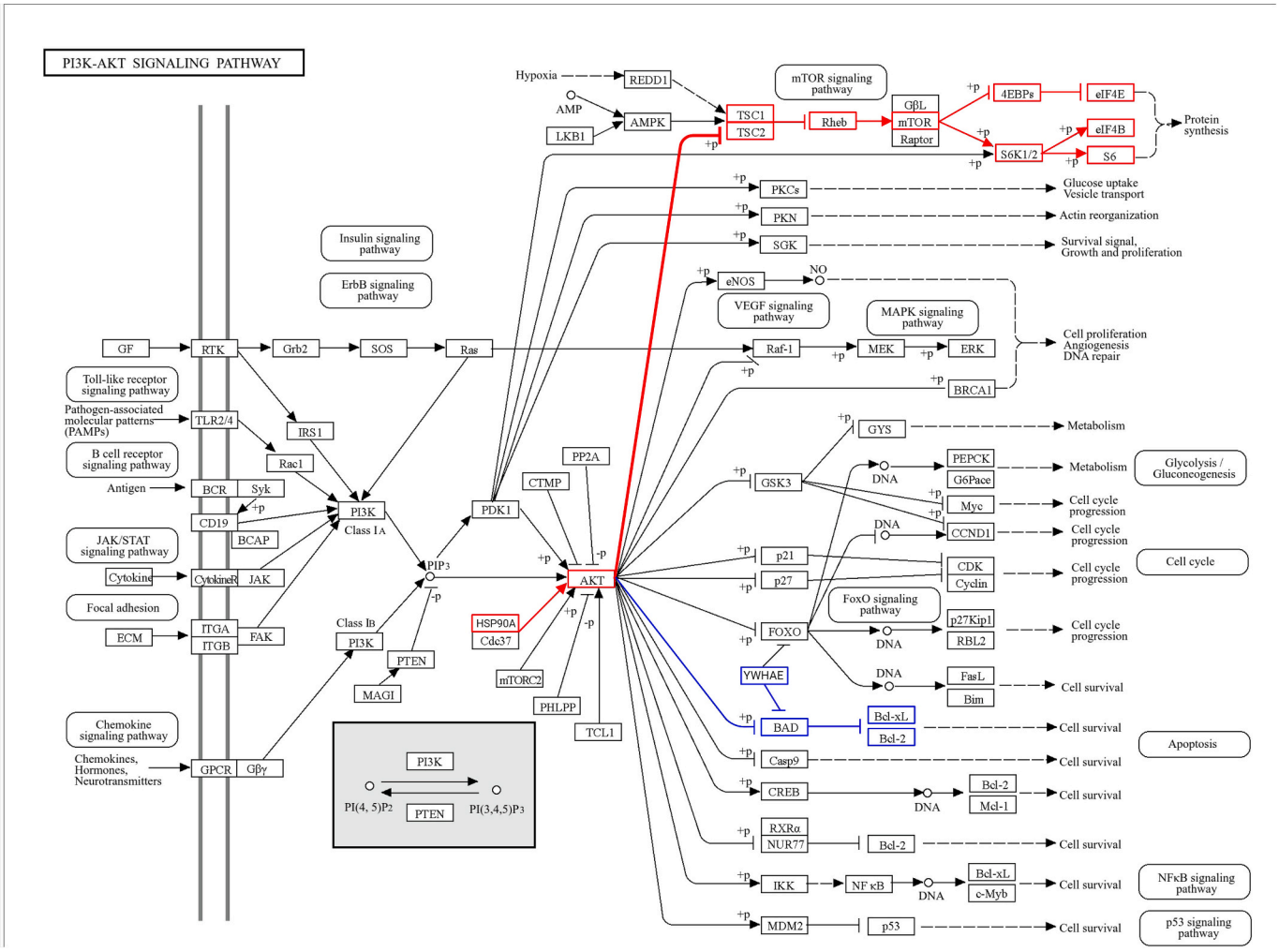


**Fig. 4.** KEGG pathway representing the PI3K-AKT signalling pathway. In response to *Mr*NV infection, heat shock protein 83 and 14–3-3 protein epsilon were significantly upregulated in *Sf9* cells, which alters the PI3K-AKT signalling pathway. (Red) PI3K-AKT-mTOR pathway is affected by many different proteins, including hsp83 (hsp90A is a human homologue). The association of hsp83 with AKT promotes phosphorylation of the tuberous sclerosis complex, which releases the inhibition of Rheb protein, activating mTOR downstream of the pathway and promoting protein synthesis. Higher levels of protein synthesis favours viral progression as it promotes viral protein synthesis. (Blue) Additionally, 14–3-3 protein epsilon (YWHAE) is involved in the AKT/BAD/Bcl-2 signalling pathway, which regulates the cell apoptosis pathway. The upregulation of YWHAE sequesters BAD protein within the cytosol, which prevents Bcl-2 protein inhibition and subsequently inhibits apoptosis. (For interpretation of the references to colour in this figure legend, the reader is referred to the web version of this article.)

delaying cell proliferation activities and enabling the host cell to prioritise the replication of viral components. Similarly, the association of 14–3-3 protein with phosphorylated cell division cycle 25 (CDC25) also confines the complex to the cytosol. CDC25, a family of phosphatases, governs the cell cycle transition from the G2 to M phase (Graves et al., 2001). Activation of CDC25 occurs through the phosphorylation of serine 216, located adjacent to the nuclear localization site (NLS), by CDC2 (Peng et al., 1997; Graves et al., 2001). This leads to the nuclear import of CDC25, initiating an autoactivation loop between CDC25 proteins (A, B, and C) and Cdk1, propelling the cell into mitosis.

Interestingly, the phosphorylation of serine 216 also reveals the adjacent 14–3-3 docking site, which is conserved in the NLS of the CDC25 family across various organisms. Binding of 14–3-3 to this docking site affects the lysine residues within the NLS, leading to a negative impact on the nuclear import of CDC25 (Dalal et al., 1999; Graves et al., 2001). While the 14–3-3 family comprises multiple forms, it is noteworthy that 14–3-3 epsilon and 14–3-3 gamma exhibit the strongest binding affinity to CDC25C (Dalal et al., 2004). Additionally, 14–3-3 protein has been found to positively regulate the activity of protein Wee1, which delays entry into mitosis by inactivating Cdk1 (Lee et al., 2001). Taken together, the synergistic mechanism involving Wee1 protein, Cdk1 inactivation, and CDC25C sequestration in the cytosol significantly contributes to cell cycle arrest at the G2 phase. The more than 2-fold increase in 14–3-3 protein epsilon expression, coupled with the cytopathic effect observed at 24 h-post-infection, underscores the role of 14–3-3 in inhibiting mitotic progression while allowing *Mr*NV to amplify its viral load. However, the unexpected slight decrease in 14–3-3 expression during the early-mid stages of infection in the *Mr*NV-infected group suggests a nuanced interaction possibly influenced by the host's interaction with *Mr*NV capsid protein, as indicated by the increased expression levels observed in the *Mr*NV VLP-invaded group.

### 4.2. *Upregulation of MrNV RNA translation initiation*

Viruses lack their own means of protein productions, necessitating the hijacking of host protein synthesis machinery, leading to competition between the hosts and the viruses. RNA viruses are generally known for their diverse effects on host translation mechanisms, which modulate ribosomes in various ways (Wang et al., 2022). Notably, one of the prominent GO annotations assigned to differentially expressed proteins was related to translation and ribosome biogenesis, commonly affected during viral infections. The alteration of both 40S and 60S ribosomal

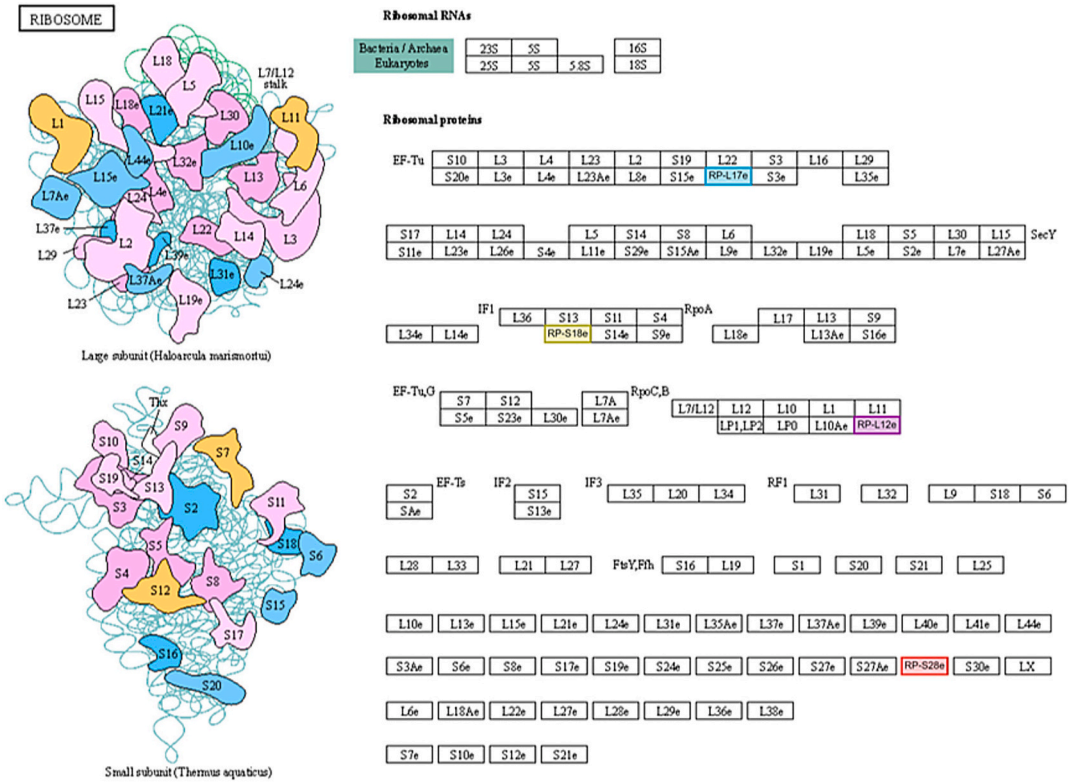


**Fig. 5.** KEGG pathway representing small and large subunits of the ribosome affected by *Macrobrachium rosenbergii* nodavirus infection. In response to *Mr*NV infection, elevated levels of 40S ribosomal subunits S18 (yellow) and S28 (red) were detected. As a result, this may promote ribosomal frameshifting and 43S sliding mechanisms for viral translation. Additionally, this increase suggests cap-dependent translation methods and internal ribosome entry site structures. Subsequently, levels 60S ribosomal subunits L12 and L17 decreased, which suggests impeding the synthesis of host proteins. (For interpretation of the references to colour in this figure legend, the reader is referred to the web version of this article.)

protein levels in *Sf*9 cells due to *Mr*NV infection (Fig. 5) suggests that *Mr*NV also impacts host ribosomes, such as the regulation of ribosomal subunits during ribosome assembly, similarly to other ssRNA viruses. *Mr*NV employs different strategies to manipulate host ribosomes, diverting from host mRNA to viral mRNA translation. These strategies include cap-dependent translation, utilising $m^7$G-capped viral mRNAs or viral cap-snatching, or cap-independent mechanisms such as viral protein linked to the genomes or internal ribosome entry sites (IRES) (Miller et al., 2021). Although nodaviruses possess a cap structure at their RNA 5′-ends, they lack a poly (A) tail at their 3′ termini (Bandin and Souto, 2020; Chen et al., 2012). Cap-dependent translation follows a canonical mechanism of infection within eukaryotic cells, initiating with the formation of a pool of 40S ribosomal subunits, followed by the association of the 5′ cap structure with eIF4F, and subsequent binding to the 40S ribosome (Sorokin et al., 2021). A set of translation initiation factors then binds onto the complex, forming the 43S pre-initiation complex. The observed increase in 40S ribosomal subunit levels throughout the late-stage *Mr*NV infection theoretically allows for a high translation initiation rate. Additionally, the increase in translational (tr)-type G domain-containing protein also points towards an increase in rates of translation initiation and elongation as tr-type G domain-containing proteins are a family of proteins that contain elongation factors, initiation factors and are stimulated by ribosomal activity (Leipe et al., 2002). Coincidentally, translationally-controlled tumour protein (TCTP) was also observed to increase in expression in response to *Mr*NV infection. TCTP is a highly conserved protein across all eukaryotic taxanomy and has been known to interact with translation elongation factors and guanine exchange factors (Bommer, 2017). A study done by Fleischer et al. (2006) revealed that the deletion of the TCTP gene in yeast caused a reduced rate of protein synthesis. As a result, tt can be postulated that *Mr*NV utilises the increase in TCTP to facilitate an increase in viral protein synthesis.We notably observed a substantial increase in 40S ribosomal subunits S18 and S28, detected at 24 h-post-infection. Intriguingly, 40S ribosomal protein S12 also exhibited elevated expression, albeit only detected 120 min post-infection during the early-mid stages, returning to baseline levels thereafter. Viral mRNAs frequently contain multiple ORFs on a single mRNA, coding for more than one protein per mRNA. As viruses rely on the host cell's translation machinery, there are mechanisms in place for viruses to translate multiple proteins from a single viral mRNA (Jaafar and Kieft, 2019). *Mr*NV RNA1 is a polycistronic viral mRNA encoding RNA-dependent RNA polymerase and B2-like protein (NaveenKumar et al., 2013). *Mr*NV likely employs ribosomal frameshifting, involving leaky scanning and 43S sliding mechanisms. Leaky scanning occurs when the start codon is flanked at positions −3 and + 4 by pyrimidines, reducing recognition, while purines, known as Kozak's context, facilitate strong recognition of the start codon (Kozak, 2002). 43S sliding occurs when the 43S complex recognizes a start codon, but the GTP bound to eIF2 does not hydrolyze, prompting the complex to continue scanning (Terenin et al., 2016).

### *4.3. Shift in 40S and 60S ribosomal subunit balance suggests two modes of translation*

Previous studies have highlighted the tight regulation of 40S and 60S ribosomal proteins, crucial for specific translational control during various cellular developmental phases (Kondrashov et al., 2011). The observed shift in the balance between these ribosomal subunits post-*Mr*NV infection suggests that *Mr*NV disrupts host ribosome biogenesis, a phenomenon common in many viral infections. Notably, studies on hepatitis C virus, a positive-sense ssRNA virus, have correlated high viral copy numbers with an abundance of 40S ribosomal subunits, while the reduction in 60S subunits did not impede viral replication. Similarly, our

**Table 2**
A list of relevant pathways detected based on the differentially expressed proteins detected between healthy, *Mr*NV VLP-invaded, and *Mr*NV-infected *Sf9* cells.

| Pathway identifier | Pathway name | Entities pValue | "-log10(p)" | Entities FDR | Submitted entities found |
|---|---|---|---|---|---|
| R-HSA-156902 | Peptide chain elongation | 6.16E-09 | 8.210380109 | 5.01E-06 | ef2;RPS28;eEF2;rpl22; Rpl12; RpS18;Rpl17 |
| R-HSA-156842 | Eukaryotic Translation Elongation | 7.20E-08 | 7.142823002 | 2.92E-05 | ef2;RPS28;eEF2;rpl22; Rpl12; RpS18;Rpl17 |
| R-HSA-72764 | Eukaryotic Translation Termination | 3.90E-07 | 6.408639208 | 6.57E-05 | RPS28;rpl22;Rpl12;RpS18; Rpl17 |
| R-HSA-72689 | Formation of a pool of free 40S subunits | 4.27E-07 | 6.369986515 | 6.57E-05 | RPS28;rpl22;Rpl12;RpS18; Rpl17 |
| R-HSA-975956 | Nonsense Mediated Decay (NMD) independent of the Exon Junction Complex (EJC) | 6.50E-07 | 6.18682335 | 6.57E-05 | RPS28;rpl22;Rpl12;RpS18; Rpl17 |
| R-HSA-156827 | L13a-mediated translational silencing of Ceruloplasmin expression | 7.62E-07 | 6.117859764 | 6.86E-05 | RPS28;rpl22;Rpl12;RpS18; Rpl17 |
| R-HSA-192823 | Viral mRNA Translation | 1.15E-06 | 5.939279588 | 9.32E-05 | RPS28;rpl22;Rpl12;RpS18; Rpl17 |
| R-HSA-72706 | GTP hydrolysis and joining of the 60S ribosomal subunit | 3.30E-06 | 5.48123632 | 2.21E-04 | RPS28;rpl22;Rpl12;RpS18; Rpl17 |
| R-HSA-927802 | Nonsense-Mediated Decay (NMD) | 8.98E-06 | 5.046544316 | 4.85E-04 | RPS28;rpl22;Rpl12;RpS18; Rpl17 |
| R-HSA-975957 | Nonsense Mediated Decay (NMD) enhanced by the Exon Junction Complex (EJC) | 8.98E-06 | 5.046544316 | 4.85E-04 | RPS28;rpl22;Rpl12;RpS18; Rpl17 |
| R-HSA-72613 | Eukaryotic Translation Initiation | 1.31E-05 | 4.88300783 | 6.15E-04 | RPS28;rpl22;Rpl12;RpS18; Rpl17 |
| R-HSA-3371497 | HSP90 chaperone cycle for steroid hormone receptors (SHR) in the presence of ligand | 3.36E-05 | 4.473737421 | 0.001410951 | TUBB3;TUBB2;Hsp90ab1; Hsp90aa1 |
| R-HSA-68877 | Mitotic Prometaphase | 5.38E-05 | 4.269110643 | 0.002076884 | YWHAE;TUBB3;TUBB2; TUBB; Hsp90aa1 |
| R-HSA-168255 | Influenza Infection | 7.74E-05 | 4.111219792 | 0.002786652 | RPS28;rpl22;Rpl12;RpS18; Rpl17;Hsp90aa1 |
| R-HSA-9711097 | Cellular response to starvation | 1.44E-04 | 3.841478708 | 0.005041843 | RPS28;rpl22;Rpl12;RpS18; Rpl17 |
| R-HSA-72766 | Translation | 4.12E-04 | 3.384794652 | 0.012368773 | ef2;RPS28;eEF2;rpl22; Rpl12; RpS18;Rpl17 |
| R-HSA-9013418 | RHOBTB2 GTPase cycle | 5.09E-04 | 3.293310711 | 0.013742098 | Hsp90ab1;Hsp90aa1 |
| R-HSA-69275 | G2/M Transition | 6.54E-04 | 3.184395677 | 0.016566396 | YWHAE;TUBB3;TUBB2; TUBB; Hsp90ab1;Hsp90aa1 |
| R-HSA-453274 | Mitotic G2-G2/M phases | 6.63E-04 | 3.178711975 | 0.016566396 | YWHAE;TUBB3;TUBB2; TUBB; Hsp90ab1;Hsp90aa1 |
| R-HSA-2262752 | Cellular responses to stress | 0.00265 | 2.576495733 | 0.03712208 | YWHAE;RPS28;rpl22; TUBB3; TUBB2;Prdx1;Rpl12; RpS18; Rpl17;Hsp90ab1; Hsp90aa1 |
| R-HSA-8953897 | Cellular responses to stimuli | 0.00292 | 2.534757195 | 0.040155008 | YWHAE;RPS28;rpl22; TUBB3; TUBB2;Prdx1;Rpl12; RpS18; Rpl17;Hsp90ab1; Hsp90aa1 |
| R-HSA-72702 | Ribosomal scanning and start codon recognition | 0.00428 | 2.368534388 | 0.051362583 | RPS28;RpS18 |
| R-HSA-9824446 | Viral Infection Pathways | 0.00451 | 2.345728774 | 0.0541318 | YWHAE;RPS28;rpl22; TUBB3; TUBB2;TUBB;Rpl12; RpS18; Rpl17;Hsp90ab1; Hsp90aa1 |
| R-HSA-68886 | M Phase | 0.00471 | 2.326923002 | 0.054464661 | YWHAE;TUBB3;TUBB2; TUBB;Hsp90aa1 |
| R-HSA-72649 | Translation initiation complex formation | 0.00877 | 2.057132226 | 0.078906046 | RPS28;RpS18 |
| R-HSA-5663205 | Infectious disease | 0.01602 | 1.795352109 | 0.128155685 | YWHAE;eEF2;TUBB; RpS18; Rpl17;Hsp90ab1; Hsp90aa1; ef2;RPS28;rpl22;TUBB3; TUBB2;Rpl12 |

The pathways were sorted by *p*-value and corrected for false discovery rate using the Benjamani-Hochberg method. The "submitted entities found" shows the list of differentially expressed proteins and closely proteins closely related that interact in those pathways and are labelled as follows, YWHAE: 14–3-3 protein epsilon, RPS28: small ribosomal protein 28, rpl22: large ribosomal protein 22, Rpl12: large ribosomal protein 12, RpS18 small ribosomal protein 18, Rpl17: large ribosomal

protein 17, TUBB3 and TUBB2: tubulin beta chain, Prdx1: peroxiredoxin 1-like isoform X1, Hsp90ab1 and Hsp90aa1: analogue of heat shock protein 83, ef2: tr-type G domain-containing protein.

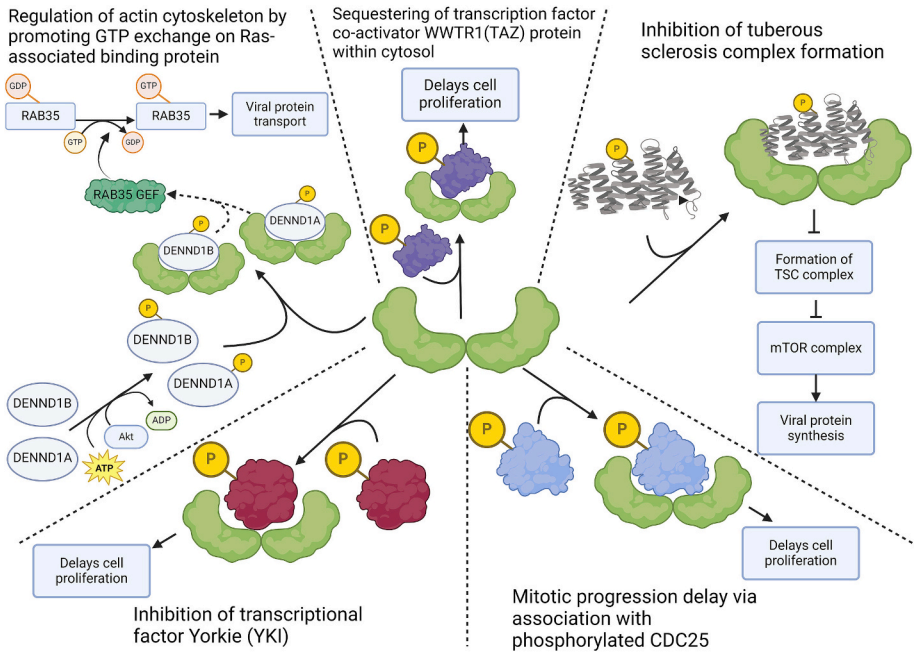


**Fig. 6.** Reactome pathway analysis of 14–3-3 protein epsilon following *Macrobrachium rosenbergii* nodavirus infection in *Sf*9. 14–3-3 protein epsilon regulates cell proliferation and cell cycle progression by binding and sequestering proteins such as TAZ, yorkie, and CDC25 within the cytosol. As a result, this inhibits cell proliferation and maintains the cell cycle progression along its G2/M phase. This suggests that *Mr*NV alters host protein production to prioritize viral proteins instead. The binding of tuberous sclerosis complex 2 (TSC2) prevents the formation of the TSC1-TSC2 complex, preventing its inhibitory effect on the mTOR pathway, which promotes viral protein production. The binding of 14–3-3 protein onto DENN domain-containing 1 stabilizes the open confirmation of the guanine exchange factor for Ras-associated binding protein (RAB), promoting GDP-GTP exchange on RAB35. Subsequently, GTP-bound RAB35 promotes the formation of actin cytoskeleton, which facilitates increased levels of viral protein transport. (The image was created using BioRender.com) (Image adapted from D'Eustachio, 2012; Orlic-Milacic et al., 2004; Orlic-Milacic et al., 2015; Rothfels, 2016; Williams, 2010).

findings indicate that the decrease in 60S ribosomal subunit L12 during the late stage and L17 during the early-mid to late stages of infection did not hinder viral replication. Although *Mr*NV mRNA typically features $m^7$G-capping, indicative of cap-dependent translation, a notable increase in 40S ribosomal subunits suggests a potential shift towards IRES-mediated, which is a cap-independent translation. This mode of translation is often upregulated in conditions where cap-dependent translation is hindered or during specific viral life cycle stages (Dobrikova et al., 2003). While it is plausible for *Mr*NV to employ both cap-dependent and cap-independent translation modes, as observed in other positive-sense ssRNA viruses, the presence of such mechanisms may hinge upon the structural characteristics of the mRNA's 5′ untranslated region (Edgil et al., 2006; Hanson et al., 2012; Fernández-García et al., 2021). IRES elements, typically located within the 5′ untranslated region (UTR) of viral genomes, may or may not be present in *Mr*NV. Previous hypotheses have suggested that even in the absence of a 5' IRES site, viral genomes can still undergo translation independently of IRES (Edgil et al., 2006). Drawing from insights into closely related viruses, it is plausible that *Mr*NV utilises both cap-independent translation methods, facilitated by interactions with the 40S ribosomal subunit and potential IRES structures, particularly evident during late-stage *Mr*NV infection.

### 4.4. Increased protein translocation and synthesis via promotion of the mTOR pathway

Actin's role in every phase of the viral life cycle is pivotal, as viruses heavily rely on its capacity to regulate and reorganize actin filaments for their benefit. In the initial stages of *Mr*NV infection, viral entry occurs through the binding of the viral capsid to a membrane receptor, initiating caveolin-mediated endocytosis to encapsulate and transport *Mr*NV into endosomes across the cytoplasm (Chen et al., 2021). As the *Mr*NV life cycle progresses, successful hijacking of host protein production facilities and increased viral replication rates necessitate the involvement of actin-related proteins for cytoplasmic trafficking (Khorramnejad et al., 2021). *Hsp90* has been identified as one of the immediate-early genes regulating white spot syndrome virus (WSSV) infection in *Litopenaeus vannamei*, where h*sp90* silencing significantly reduces WSSV copy numbers, while elevated *hsp90* levels enhance WSSV infection (Yingsunthonwattana et al., 2022). Other RNA viruses exploit host hsp90 to bolster their replication while impeding host protein translation (Wan et al., 2020). The elevated levels of heat shock protein in *Sf*9 cells during the early to mid-stages, along with consistent actin expression throughout all infection stages, align precisely with expectations for *Mr*NV infection. KEGG pathway analysis of hsp83 suggests potential modulation of the PI3K/AKT/mTOR pathway during *Mr*NV infection.

The phosphorylation of TSC2 subsequent to *Mr*NV VLP invasion releases its inhibitory effect on mTOR, thereby facilitating downstream protein translation. Our observations of an increase in hsp83 (an insect homologue of hsp90) during the early to mid-stages of infection in *Mr*NV VLP-invaded and *Mr*NV-infected *Sf*9 cells likely stem from the interaction between *Mr*NV capsid protein and the host signalling pathway (Straten et al., 1997). We propose this theory based on the limited extent of *Mr*NV VLP invasion, which is primarily mediated by the *Mr*NV capsid protein. This protein lacks the capability to produce other viral proteins or replicate within *Sf*9 cells due to genetic constraints. As infection progresses, we observed a decrease in hsp83 levels in *Mr*NV VLP-

invaded *Sf*9 cells compared to those infected with *Mr*NV, possibly indicating *Mr*NV proficiency at sustaining the infection. Reactome analysis of the differentially expressed 14–3-3 protein epsilon suggests its involvement in regulating the Ras-associated binding (RAB) protein signalling pathway in *D. melanogaster*, a pathway crucial for actin regulation and cytoskeletal rearrangement. Binding of 14–3-3 dimer onto CG30347 (a homologue of human DENN domain-containing protein 1 A) stabilizes the open confirmation of RAB GTP-exchange factors (GEFs), promoting the release of GDP from RAB35 and facilitating GTP binding (Kulasekaran et al., 2015; Marat et al., 2011). Downstream effects of GTP-bound RAB35 include actin regulation through fascin recruitment, a known actin-bundling factor studied in closely related species such as *Spodoptera exigua* (Ahmed and Kim, 2019; Kouranti et al., 2006; Zhang et al., 2009). Furthermore, the Reactome pathway browser predicted that 14–3-3 protein epsilon detected in *D. melanogaster* binds phosphorylated TSC2, sequestering it to the cytosol and preventing its association with TSC1 (Liu et al., 2002; Cai et al., 2006), consequently inhibiting the mTOR signalling pathway. Collectively, 14–3-3 protein epsilon has been recognized as a proviral factor in various viruses affecting different species (Aoki et al., 2000; Cao et al., 2019; Kino et al., 2005).

### 4.5. Promotion of apoptosis through peroxiredoxin downregulation

Hydrogen peroxide ($H_2O_2$) serves as a pivotal signalling molecule, orchestrating various cellular processes including the cell cycle, differentiation, and apoptosis (Heo et al., 2020). $H_2O_2$ is a byproduct of normal cellular metabolism in mitochondria, and excessive levels can be cytotoxic. In response, cells produce peroxiredoxins, thiol peroxidases that rapidly reduce $H_2O_2$, thus thwarting apoptosis induction (Nagy et al., 2011; Xiang et al., 2016). Peroxiredoxins also play a positive role in antiviral pathways; for instance, peroxiredoxin-1 has been implicated in reducing hepatitis B virus (HBV) RNA levels post-transcriptionally, thereby impeding HBV propagation (Deng et al., 2019). Additionally, peroxiredoxin-6 exhibits antiviral properties by suppressing the replication of porcine picornavirus Senecavirus A (SVA) and foot-and-mouth disease virus (FMDV) (Wang et al., 2021). However, recent studies have revealed that SVA and FMDV possess mechanisms to degrade peroxiredoxins via viral protease $3C^{pro}$ expression. While certain viruses can counteract the antiviral effects of peroxiredoxins, the specific antiviral functions of these proteins, especially in the context of insect and aquaculture viruses, remain largely unexplored, leaving us to speculate based solely on changes in their expression levels.

In our study, we observed differential expression of peroxiredoxin 1-like isoform X1 in *Mr*NV-infected *Sf*9 cells, showing decreased expression during late-stage infection. The notable population of cells exhibiting extreme vacuolation and blebbing characteristics 24 h post-infection (Fig. 1l) correlates with the decrease in peroxiredoxin levels detected in our proteomics data. This decline in peroxiredoxin expression during late-stage *Mr*NV infection suggests that the virus may elevate $H_2O_2$ levels to induce apoptosis for viral propagation. However, further investigations are warranted to confirm this correlation, and fully elucidate the impact of decreased peroxiredoxin 1-like isoform X1 expression on *Mr*NV infection.

## 5. Strengths, limitations, and future perspectives

Mass-spectrometry-based proteomics is a powerful tool for understanding protein expression changes in response to infection. Given the scarcity of protein databases covering changes in its primary host organism, *M. rosenbergii,* one strength of our approach was the utilisation of *Sf*9, a well-known insect cell model. By leveraging existing databases, we enabled protein identification based on shared derived traits along the host's phylogenetic tree. Additionally, our work represents the first proteomic profiling of protein changes during *Mr*NV infection. Previous studies on *Mr*NV infection relied on transcriptomic approaches, which, while informative, may not correlate with protein expression changes.

However, our study has some limitations. Firstly, the use of *Sf9* cell model, although susceptible to *Mr*NV, may not fully replicate the complexities of infection within shrimp cells or whole organisms. Nonetheless, shrimp cell models are notoriously difficult to culture and expensive (Chen et al., 2021). Furthermore, *in vivo* proteomics experiments in *M. rosenbergii* are challenging due to protein variability and the lack of a comprehensive protein database for the organism. Currently, there are only 1139 proteins in the *M. rosenbergii* database compared to 57,037 proteins in the *Sf9* database, and 1,936,877 proteins in the *Homo sapiens* database (Schoch et al., 2020).

## 6. Conclusion

Our current understanding of the mechanism of *Mr*NV infection remains inadequate, posing challenges in devising treatments and preventive strategies against WTD. In this study, we adopted a bottom-up proteomics approach to elucidate the dynamics of protein expression changes as *Mr*NV progresses from early to late stages of infection in *Sf*9 cells. Our findings indicate that *Mr*NV manipulated the host's protein production machinery as early as 120 min post-infection, positioning it between the early to mid-stages of infection. The upregulation of hsp83 during the early infection phase may facilitate *Mr*NV establishment by enhancing the mTOR pathway. Concurrently, the sustained upregulation of the tubulin beta chain suggests heightened protein translocation and actin rearrangement throughout infection progression. Notably, alterations in protein expression during the early to mid-stages of infection appear to be influenced by interactions involving the *Mr*NV capsid, underscoring its significance in the infection process.

Furthermore, our results suggest that *Mr*NV impedes cellular growth and disrupts cell cycle progression through the upregulation of 14–3-3 protein epsilon. Coupled with our morphological observations 24-h post-*Mr*NV infection, the decline in peroxiredoxin levels during the later infection stages indicates substantial cell lysis. The identified pathway alterations during *Mr*NV infection represent potential therapeutic targets. For instance, the development of competitive inhibitors targeting specific 14–3-3 protein subunits could restore normal cell cycle progression during the viral infection. Looking ahead, conducting proteomic investigations using an *in vivo* model, particularly *M. rosenbergii* post-larvae, would offer valuable insights as it closely mirrors natural infection scenarios. Overall, our study provides significant insights into the mechanisms of *Mr*NV infectivity, laying the groundwork for future therapeutic advancements against this viral disease.

## CRediT authorship contribution statement

**Ken Fong Chen:** Writing – review & editing, Writing – original draft, Methodology, Investigation, Formal analysis, Data curation. **Wen Siang Tan:** Writing – review & editing, Supervision, Funding acquisition. **Lin Kooi Ong:** Writing – review & editing, Supervision. **Syafiq Asnawi Zainal Abidin:** Writing – review & editing, Supervision. **Iekhsan Othman:** Writing – review & editing, Funding acquisition. **Beng Ti Tey:** Writing – review & editing, Funding acquisition. **Ronald Fook Seng Lee:** Writing – review & editing, Writing – original draft, Funding acquisition, Conceptualization.

## Declaration of competing interest

The authors declare that they have no known competing financial interests or personal relationships that could have appeared to influence the work reported in this paper.

## Data availability

Data will be made available on request.

## Acknowledgements

The work is funded by the Fundamental Research Grant Scheme (FRGS/1/2019/STG04/MUSM/03/2), Ministry of Higher Education, Malaysia.

## Appendix A. Supplementary data

Supplementary data to this article can be found online at https://doi.org/10.1016/j.aquaculture.2024.741915.

## References

Ahmed, S., Kim, Y., 2019. PGE2 mediates cytoskeletal rearrangement of hemocytes via Cdc42, a small G protein, to activate actin-remodeling factors in *Spodoptera exigua* (Lepidoptera: Noctuidae). Arch. Insect Biochem. Physiol. 102, e21607. https://doi.org/10.1002/arch.21607.

Aoki, H., Hayashi, J., Moriyama, M., Arakawa, Y., Hino, O., 2000. Hepatitis C virus Core protein interacts with 14-3-3 protein and activates the kinase Raf-1. J. Virol. 74, 1736–1741. https://doi.org/10.1128/2Fjvi.74.4.1736-1741.2000.

Arcier, J.-M., Herman, F., Lightner, D.V., Redman, R.M., Mari, J., 1999. A viral disease associated with mortalities in hatchery-reared postlarvae of the giant freshwater prawn *Macrobrachium rosenbergii*. Dis. Aquat. Org. 38, 177–181. https://doi.org/10.3354/dao038177.

Ashburner, M., Ball, C.A., Blake, J.A., Botstein, D., Butler, H., Cherry, J.M., Davis, A.P., Dolinski, K., Dwight, S.S., Eppig, J.T., Harris, M.A., Hill, D.P., Issel-Tarver, L., Kasarskis, A., Lewis, S., Matese, J.C., Richardson, J.E., Ringwald, M., Rubin, G.M., Sherlock, G., 2000. Gene ontology: tool for the unification of biology. Nat. Genet. 25, 25–29. https://doi.org/10.1038/75556.

Bandin, I., Souto, S., 2020. Betanodavirus and VER disease: a 30-year research review. Pathogens 9, 106. https://doi.org/10.3390/2Fpathogens9020106.

Barber, G.N., 2001. Host defense, viruses and apoptosis. Cell Death Differ. 8, 113–126. https://doi.org/10.1038/sj.cdd.4400823.

Bommer, U.A., 2017. The translational controlled tumour protein TCTP: biological functions and regulation. In: Telerman, A., Amson, R. (Eds.), TCTP/tpt1 - Remodeling Signaling from Stem Cell to Disease. Results and Problems in Cell Differentiation, 64. Springer, Cham. https://doi.org/10.1007/978-3-319-67591-6_4.

Bradford, M.M., 1976. A rapid and sensitive method for the quantitation of microgram quantities of protein utilizing the principle of protein-dye binding. Anal. Biochem. 72, 248–254. https://doi.org/10.1006/abio.1976.9999.

Cai, S.-L., Tee, A.R., Short, J.D., Bergeron, J.M., Kim, J., Shen, J., 2006. Activity of TSC2 is inhibited by AKT-mediated phosphorylation and membrane partitioning. J. Cell Biol. 173, 279–289. https://doi.org/10.1083/jcb.200507119.

Cao, S., Cong, F., Tan, M., Ding, G., Liu, J., Li, L., Zhao, Y., Liu, S., Xiao, Y., 2019. 14-3-3ε acts as a proviral factor in highly pathogenic porcine reproductive and respiratory syndrome virus infection. Vet. Res. 50, 16. https://doi.org/10.1186/s13567-019-0636-0.

Chen, Y.P., Becnel, J.J., Valles, S.M., 2012. Chapter 5 - RNA viruses infecting Pest insects. In: Vega, F.E., Kaya, H.K., Second, E. (Eds.), Insect Pathology, vol. 2. Academic Press, San Diego, California, pp. 133–170. https://doi.org/10.1016/B978-0-12-384984-7.00005-1.

Chen, K.F., Tan, W.S., Ong, L.K., Zainal Abidin, S.A., Othman, I., Tey, B.T., Lee, R.F.S., 2021. The Macrobrachium rosenbergii nodavirus: a detailed review of structure, infectivity, host immunity, diagnosis and prevention. Rev. Aqucult. 13, 2117–2141. https://doi.org/10.1111/raq.12562.

Chen, K.F., Maran, S., Tan, W.S., Ong, L.K., Zainal Abidin, S.A., Othman, I., Tey, B.T., Lee, R.F.S., 2023. Meta-analysis of studies on protection provided by different prophylactic agents, their routes of administration and incubation times against nodavirus infection in *Macrobrachium rosenbergii*. Aquaculture 565, 739125. https://doi.org/10.1016/j.aquaculture.2022.739125.

Dalal, S.N., Schweitzer, C.M., Gan, J., DeCaprio, J.A., 1999. Cytoplasmic localization of human cdc25C during interphase requires an intact 14-3-3 binding site. Mol. Cell. Biol. 19, 4465–4479. https://doi.org/10.1128/2Fmcb.19.6.4465.

Dalal, S.N., Yaffe, M.B., DeCaprio, J.A., 2004. 14-3-3 family members act coordinately to regulate mitotic progression. Cell Cycle 3, 670–675. https://doi.org/10.4161/cc.3.5.856.

Davy, C., Doorbar, J., 2007. G2/M cell cycle arrest in the life cycle of viruses. Virology 368, 219–226. https://doi.org/10.1016/j.virol.2007.05.043.

Deng, L., Gan, X., Ito, M., Chen, M., Aly, H.H., Matsui, C., Abe, T., Watashi, K., Wakita, T., Suzuki, T., Okamoto, T., Matsuura, Y., Mizokami, M., Shoji, I., Hotta, H., 2019. Peroxiredoxin 1, a novel HBx-interacting protein, interacts with exosome component 5 and negatively regulates hepatitis B virus (HBV) propagation through degradation of HBV RNA. J. Virol. 93, e02203–e02218. https://doi.org/10.1128/jvi.02203-18.

D'Eustachio, P., 2012. Signalling by Hippo. *Reactome*, Release 87. https://doi.org/10.3180/REACT_118607.1. Retrieved [01-03-2024].

Dobrikova, E., Florez, P., Bradrick, S., Gromeier, M., 2003. Activity of a type 1 picornavirus internal ribosomal entry site is determined by sequences within the 3′ nontranslated region. Proc. Natl. Acad. Sci. U. S. A. 100, 15125–15130. https://doi.org/10.1073/pnas.2436464100.

Edgil, D., Polacek, C., Harris, E., 2006. Dengue virus utilizes a novel strategy for translation initiation when cap-dependent translation is inhibited. J. Virol. 80, 2976–2986. https://doi.org/10.1128/jvi.80.6.2976-2986.2006.

Fabregat, A., Sidiropoulos, K., Viteri, G., Forner, O., Marin-Garcia, P., Arnau, V., D'Eustachio, P., Stein, L., Hermjakob, H., 2017. Reactome pathway analysis: a high-performance in-memory approach. BMC Bioinformatics. 18, 142. https://doi.org/10.1186/s12859-017-1559-2.

Fernández-García, L., Angulo, J., Ramos, H., Barrera, A., Pino, K., Vera-Otarola, J., López-Lastra, M., 2021. The internal ribosome entry site of dengue virus mRNA is active when cap-dependent translation initiation is inhibited. J. Virol. 95. https://doi.org/10.1128/jvi.01998-20 e01998–20.

Flather, D., Semler, B.L., 2015. Picornaviruses and nuclear functions: targeting a cellular compartment distinct from the replication site of a positive-strand RNA virus. Front. Microbiol. 6, 594. https://doi.org/10.3389/fmicb.2015.00594.

Fleischer, T.C., Weaver, C.M., McAfee, K.J., Jennings, J.L., Link, A.J., 2006. Systematic identification and functional screens of uncharacterized proteins associated with eukaryotic ribosomal complexes. Genes Dev. 20, 1294–1307. https://doi.org/10.1101/gad.1422006.

Food and Agriculture, 2021. Global production by production source 1950–2021 (FishStatJ). In: FAO Fisheries and Aquaculture Division [online] (2021) Rome. Updated 2023.

Goh, Z.H., Tan, S.G., Bhassu, S., Tan, W.S., 2011. Virus-like particles of *Macrobrachium rosenbergii* nodavirus produced in bacteria. J. Virol. Methods 175, 74–79. https://doi.org/10.1016/j.jviromet.2011.04.021.

Goh, Z.H., Mohd, N.A.S., Tan, S.G., Bhassu, S., Tan, W.S., 2014. RNA-binding region of *Macrobrachium rosenbergii* nodavirus capsid protein. J. Gen. Virol. 95, 1919–1928. https://doi.org/10.1099/vir.0.064014-0.

Graves, P., Lovely, C., Uy, G., Piwnica-Worms, H., 2001. Localization of human Cdc25C is regulated both by nuclear export and 14-3-3 protein binding. Oncogene 20, 1839–1851. https://doi.org/10.1038/sj.onc.1204259.

Gunawardana, Y., Niranjan, M., 2013. Bridging the gap between transcriptome and proteome measurements identifies post-translationally regulated genes. Bioinformatics 29, 3060–3066. https://doi.org/10.1093/bioinformatics/btt537.

Hanapi, U.F., Yong, C.Y., Goh, Z.H., Alitheen, N.B., Yeap, S.K., Tan, W.S., 2017. Tracking the virus-like particles of *Macrobrachium rosenbergii* nodavirus in insect cells. PeerJ 5, e2947. https://doi.org/10.7717/2Fpeerj.2947.

Hanson, G., Coller, J., 2017. Codon optimality, bias and usage in translation and mRNA decay. Nat. Rev. Mol. Cell Biol. 19, 20–30. https://doi.org/10.1038/nrm.2017.91.

Hanson, P.J., Zhang, H.M., Hemida, M.G., Ye, X., Qiu, Y., Yang, D., 2012. IRES-dependent translational control during virus-induced endoplasmic reticulum stress and apoptosis. Front. Microbiol. 3. https://doi.org/10.3389/2Ffmicb.2012.00092.

Heo, S., Kim, S., Kang, D., 2020. The role of hydrogen peroxide and peroxiredoxins throughout the cell cycle. Antioxidants 9, 280. https://doi.org/10.3390/antiox9040280.

Israels, E.D., Israels, L.G., 2000. The cell cycle. Oncologist 5, 510–513. https://doi.org/10.1634/theoncologist.5-6-510.

Jaafar, Z.A., Kieft, J.S., 2019. Viral RNA structure-based strategies to manipulate translation. Nat. Rev. Microbiol. 17, 110–123. https://doi.org/10.1038/s41579-018-0117-x.

Jariyapong, P., Pudgerd, A., Weerachatyanukul, W., Hirono, I., Senapin, S., Dhar, A.K., Chotwiwatthanakun, C., 2018. Construction of an infectious *Macrobrachium rosenbergii* nodavirus from cDNA clones in *Sf*9 cells and improved recovery of viral RNA with AZT treatment. Aquaculture 483, 111–119. https://doi.org/10.1016/j.aquaculture.2017.10.008.

Kanehisa, M., Goto, S., 2000. KEGG: Kyoto Encyclopedia of Genes and Genomes, 28. Oxford University Press, pp. 27–30. https://doi.org/10.1093/2Fnar/2F28.1.27.

Khorramnejad, A., Perdomo, H.D., Palatini, U., Bonizzoni, M., Gasmi, L., 2021. Cross talk between viruses and insect cells cytoskeleton. Viruses 13, 1658. https://doi.org/10.3390/v13081658.

Kino, T., Gragerov, A., Valentin, A., Tsopanomihalou, M., Ilyina-Gragerova, G., Erwin-Cohen, R., Chrousos, G.P., Pavlakis, G.N., 2005. Vpr protein of human immunodeficiency virus type 1 binds to 14–3-3 proteins and facilitates complex formation with Cdc25C: implications for cell cycle arrest. J. Virol. 79, 2780–2787. https://doi.org/10.1128/jvi.79.5.2780-2787.2005.

Kondrashov, N., Pusic, A., Stumpf, C.R., Shimizu, K., Hsieh, A.C., Ishijima, J., Shiroishi, T., Maria, B., 2011. Ribosome-mediated specificity in Hox mRNA translation and vertebrate tissue patterning. Cell 145, 383–397. https://doi.org/10.1016/j.cell.2011.03.028.

Kouranti, I., Sachse, M., Arouche, N., Goud, B., Echard, A., 2006. Rab35 regulates an endocytic recycling pathway essential for the terminal steps of cytokinesis. Curr. Biol. 16, 1719–1725. https://doi.org/10.1016/j.cub.2006.07.020.

Kozak, M., 2002. Pushing the limits of the scanning mechanism for initiation of translation. Gene 299, 1–34. https://doi.org/10.1016/S0378-1119(02)01056-9.

Kulasekaran, G., Nossova, N., Marat, A.L., Lund, I., Cremer, C., Ioannou, M.S., McPherson, P.S., 2015. Phosphorylation-dependent regulation of Connecdenn/DENND1 guanine nucleotide exchange factors. J. Biol. Chem. 290, 17999–18008. https://doi.org/10.1074/jbc.m115.636712.

Lee, J., Kumagai, A., Dunphy, W.G., 2001. Positive regulation of Wee1 by Chk1 and 14-3-3 proteins. Mol. Biol. Cell 12, 551–563. https://doi.org/10.1091/mbc.12.3.551.

Leipe, D.D., Wolf, Y.I., Koonin, E.V., Aravind, L., 2002. Classification and evolution of P-loop GTPases and related ATPases. J. Mol. Biol. 317, 41–72. https://doi.org/10.1006/jmbi.2001.5378.

Liou, J.-Y., Lee, S., Ghelani, D., Matijevic-Aleksic, N., Wu, K.K., 2006. Protection of endothelial survival by peroxisome proliferator-activated receptor-δ mediated 14-3-3 upregulation. Arterioscler. Thromb. Vasc. Biol. 26, 1481–1487. https://doi.org/10.1161/01.atv.0000223875.14120.93.

Liu, M.Y., Cai, S., Espejo, A., Bedford, M.T., Walker, C., 2002. 14-3-3 interacts with the tumor suppressor tuberin at Akt phosphorylation site(s). Cancer Res. 62, 6475–6480.
Marat, A.L., Dokainish, H., McPherson, P.S., 2011. DENN domain proteins: regulators of Rab GTPases. J. Biol. Chem. 286, 13791–13800. https://doi.org/10.1074/jbc.r110.217067.
Miller, C.M., Selvam, S., Fuchs, G., 2021. Fatal attraction: the roles of ribosomal proteins in the viral life cycle. WIREs RNA 12, e1613. https://doi.org/10.1002/2Fwrna.1613.
Mubeen, S., Hoyt, C.T., Gemünd, A., Hofmann-Apitius, M., Fröhlich, H., Domingo-Fernández, D., 2019. The impact of pathway database choice on statistical enrichment analysis and predictive modeling. Sec. Front Genet. 10, 1203. https://doi.org/10.3389/fgene.2019.01203.
Nagy, P., Karton, A., Betz, A., Peskin, A.V., Pace, P., O'Reilly, R.J., 2011. Model for the exceptional reactivity of peroxiredoxins 2 and 3 with hydrogen peroxide. J. Biol. Chem. 286, 18048–18055. https://doi.org/10.1074/jbc.M111.232355.
NaveenKumar, S., Shekar, M., Karunasagar, I., Karunasagar, I., 2013. Genetic analysis of RNA1 and RNA2 of *Macrobrachium rosenbergii* nodavirus (*Mr*NV) isolated from India. Virus Res. 173, 377–385. https://doi.org/10.1016/j.virusres.2013.01.003.
Neymotin, B., Ettorre, V., Gresham, D., 2016. Multiple transcript properties related to translation affect mRNA degradation rates in *Saccharomyces cerevisiae*. G3 (Bethesda) 6, 3475–3483. https://doi.org/10.1534/2Fg3.116.032276.
Orlic-Milacic, M., Borowiec, J.A., Matthews, L., Sanchez, Y., 2004. G2/M checkpoints. Reactome 87. https://doi.org/10.3180/REACT_828.2. Release. Retrieved [01-03-2024].
Orlic-Milacic, M., Makela, T., Katajisto, P., Wu, J., Jassal, B., May, B., D'Eustachio, P., Nasi, S., Annibali, D., Schmidt, E., Matthews, L., Pagano, M., Khanna, K.K., 2015. Transcriptional regulation by TP53. Reactome 87. https://doi.org/10.3180/r-hsa-3700989.4. Retrieved [01-03-2024]. Release.
Pasookhush, P., Hindmarch, C., Sithigorngul, P., Longyant, S., Bendena, W.G., Chaivisuthangkura, P., 2019. Transcriptomic analysis of *Macrobrachium rosenbergii* (giant fresh water prawn) post-larvae in response to *M. rosenbergii* nodavirus (*Mr*NV) infection: de novo assembly and functional annotation. BMC Genomics 20, 762. https://doi.org/10.1186/s12864-019-6102-6.
Peng, C.-Y., Graves, P.R., Thoma, R.S., Wu, Z., Shaw, A.S., Piwnica-Worms, H., 1997. Mitotic and G2 checkpoint control: regulation of 14-3-3 protein binding by phosphorylation of Cdc25C on Serine-216. Science 277, 1501–1505. https://doi.org/10.1126/science.277.5331.1501.
Rohrmann, G.F., 2019. Chapter 7, Baculovirus infection: the cell cycle and apoptosis. In: Baculovirus Molecular Biology [Internet], 4th edition. National Center for Biotechnology Information (US), Bethesda (MD).
Rothfels, K., 2016. RAB GEFs exchange GTP for GDP on RABs. Reactome. https://doi.org/10.3180/R-HSA-8876198.1. Retrieved [01-03-2024].
Schoch, C.L., Ciufo, S., Domrachev, M., Hotton, C.L., Kannan, S., Khovanskaya, R., Leipe, D., Mcveigh, R., O'Neill, K., Robbertse, B., Sharma, S., Soussov, V., Sullivan, J. P., Sun, L., Turner, S., Karsch-Mizrachi, I., 2020. NCBI taxonomy: a comprehensive update on curation, resources and tools. Database. https://doi.org/10.1093/database/baaa062. : the journal of biological databases and curation. baaa062.
Sirikharin, R., Utairungsee, T., Srisala, J., Roytrakul, S., Thitamadee, S., Sritunyalucksana, K., 2019. Cell surface transglutaminase required for nodavirus entry into freshwater prawn hemocytes. Fish Shellfish Immunol. 89, 108–116. https://doi.org/10.1016/j.fsi.2019.03.052.
Somrit, M., Watthammawut, A., Chotwiwatthanakun, C., Weerachatyanukul, W., 2016. The key molecular events during *Macrobrachium rosenbergii* nodavirus (*Mr*NV) infection and replication in *Sf*9 insect cells. Virus Res. 223, 1–9. https://doi.org/10.1016/j.virusres.2016.06.012.
Sorokin, I.I., Vassilenko, K.S., Terenin, I.M., Kalinina, N.O., Agol, V.I., Dmitriev, S.E., 2021. Non-canonical translation initiation mechanisms employed by eukaryotic viral mRNAs. Biochemistry (Mosc) 86, 1060–1094. https://doi.org/10.1134/s0006297921090042.
Straßburger, K., Tiebe, M., Pinna, F., Breuhahn, K., Teleman, A.A., 2012. Insulin/IGF signaling drives cell proliferation in part via Yorkie/YAP. Dev. Biol. 367, 187–196. https://doi.org/10.1016/j.ydbio.2012.05.008.
Straten, A.V.D., Rommel, C., Dickson, B., Hafen, E., 1997. The heat shock protein 83 (Hsp83) is required for Raf-mediated signalling in *Drosophila*. EMBO J. 16, 1961–1969. https://doi.org/10.1093/emboj/16.8.1961.
Subramanian, R.R., Masters, S.C., Zhang, H., Fu, H., 2001. Functional conservation of 14-3-3 isoforms in inhibiting bad-induced apoptosis. Exp. Cell Res. 271, 142–151. https://doi.org/10.1006/excr.2001.5376.
Takemon, Y., Chick, J.M., Gyuricza, I.G., Skelly, D.A., Devuyst, O., Gygi, S.P., Churchill, G.A., Korstanje, R., 2021. Proteomic and transcriptomic profiling reveal different aspects of aging in the kidney. eLife 10, e62585. https://doi.org/10.7554/eLife.62585.
Terenin, I.M., Akulich, K.A., Andreev, D.E., Polyanskaya, S.A., Shatsky, I.N., Dmitriev, S. E., 2016. Sliding of a 43S ribosomal complex from the recognized AUG codon triggered by a delay in eIF2-bound GTP hydrolysis. Nucleic Acids Res. 44, 1882–1893. https://doi.org/10.1093/nar/gkv1514.
The Gene Ontology Consortium, 2023. The gene ontology knowledgebase in 2023. Genetics 224. https://doi.org/10.1093/genetics/iyad031 iyad031.
Wan, Q., Song, D., Li, H., He, M.-l., 2020. Stress proteins: the biological functions in virus infection, present and challenges for target-based antiviral drug development. Sig Transduct. Target Ther. 5, 125. https://doi.org/10.1038/s41392-020-00233-4.
Wang, H.-C., Wang, H.-C., Leu, J.-H., Kou, G.-H., Wang, A.H.-J., Lo, C.-F., 2007. Protein expression profiling of the shrimp cellular response to white spot syndrome virus infection. Dev. Comp. Immunol. 31, 672–686. https://doi.org/10.1016/j.dci.2006.11.001.
Wang, L., Chen, Z., Wang, Y., Chang, D., Su, L., Guo, Y., Liu, C., 2014. TR1 promotes cell proliferation and inhibits apoptosis through cyclin A and CTGF regulation in non-small cell lung cancer. Tumour Biol. 35, 463–468. https://doi.org/10.1007/s13277-013-1064-9.
Wang, C., Feng, H., Zhang, X., Li, K., Yang, F., Cao, W., Liu, H., Gao, L., Xue, Z., Liu, X., Zhu, Z., Zheng, H., 2021. Porcine picornavirus 3C protease degrades PRDX6 to impair PRDX6-mediated antiviral function. Virol. Sin. 36, 948–957. https://doi.org/10.1007/2Fs12250-021-00352-4.
Wang, J., Sun, D., Wang, M., Cheng, A., Zhu, Y., Mao, S., Qu, X., Zhao, X., Huang, J., Gao, Q., Zhang, S., Yang, Q., Wu, Y., Zhu, D., Jia, R., Chen, S., Liu, M., 2022. Multiple functions of heterogeneous nuclear ribonucleoproteins in the positive single-stranded RNA virus life cycle. Front. Immunol. 13, 989298. https://doi.org/10.3389/2Ffimmu.2022.989298.
Williams, M.G., 2010. Hippo/warts pathway. Reactome. https://doi.org/10.3180/REACT_23433.1. Retrieved [01-03-2024].
Xiang, J., Wan, C., Guo, R., Guo, D., 2016. Is hydrogen peroxide a suitable apoptosis inducer for all cell types? Biomed. Res. Int. 2016, 7343965. https://doi.org/10.1155/2F2016/2F7343965.
Yingsunthonwattana, W., Junprung, W., Supungul, P., Tassanakajon, A., 2022. Heat shock protein 90 of Pacific white shrimp (*Litopenaeus vannamei*) is possibly involved in promoting white spot syndrome virus infection. Fish Shellfish Immunol. 128, 405–418. https://doi.org/10.1016/j.fsi.2022.08.016.
Zainal Abidin, S.A., Rajadurai, P., Chowdhury, M.E., Ahmad Rusmili, M.R., Othman, I., Naidu, R., 2016. Proteomic characterization and comparison of Malaysian *Tropidolaemus wagleri* and *Cryptelytrops purpureomaculatus* venom using shotgun-proteomics. Toxins 8, 299. https://doi.org/10.3390/toxins8100299.
Zhang, J., Fonovic, M., Suyama, K., Bogyo, M., Scott, M.P., 2009. Rab35 controls actin bundling by recruiting Fascin as an effector protein. Science 325, 1250–1254. https://doi.org/10.1126/science.1174921.